Ghost imaging: from quantum to classical to computational

Baris I. Erkmen[1,*] and Jeffrey H. Shapiro[2]

[1]Jet Propulsion Laboratory, California Institute of Technology, 4800 Oak Grove Drive Pasadena, California 91109, USA

[2]Research Laboratory of Electronics, Massachusetts Institute of Technology, 77 Massachusetts Avenue, Cambridge, Massachusetts 02139, USA

*Corresponding author: baris.i.erkmen@jpl.nasa.gov

Received March 29, 2010; revised July 19, 2010; accepted July 27, 2010; published August 20, 2010 (Doc. ID 126211)

Ghost-imaging experiments correlate the outputs from two photodetectors: a high-spatial-resolution (scanning pinhole or CCD array) detector that measures a field that has not interacted with the object to be imaged, and a bucket (single-pixel) detector that collects a field that has interacted with the object. We give a comprehensive review of ghost imaging—within a unified Gaussian-state framework—presenting detailed analyses of its resolution, field of view, image contrast, and signal-to-noise ratio behavior. We consider three classes of illumination: thermal-state (classical), biphoton-state (quantum), and classical-state phase-sensitive light. The first two have been employed in a variety of ghost-imaging demonstrations. The third is the classical Gaussian state that produces ghost images that most closely mimic those obtained from biphoton illumination. The insights we develop lead naturally to a new, single-beam approach to ghost imaging, called computational ghost imaging, in which only the bucket detector is required. We provide quantitative results while simultaneously emphasizing the underlying physics of ghost imaging. The key to developing the latter understanding lies in the coherence behavior of a pair of Gaussian-state light beams with either phase-insensitive or phase-sensitive cross correlation.

OCIS codes: 110.4980, 270.5290, 030.1640, 110.1758.

1943-8206/10/040405-46/$15.00

Ghost imaging: from quantum to classical to computational

Baris I. Erkmen and Jeffrey H. Shapiro

1. Introduction

Ghost imaging is a transverse imaging modality that has been receiving considerable and increasing attention of late, owing to its novel physical characteristics. Aside from minor implementation variations, virtually all ghost-imaging demonstrations thus far exploit the cross correlation between the photocurrents obtained from illumination of two spatially separated photodetectors by a pair of highly correlated optical beams. One beam interrogates a target (or sample) and then illuminates a single-pixel (bucket) detector that provides no spatial resolution. The other beam does not interact with the target, but it impinges on a scanning pinhole detector or a high-resolution camera, hence affording a multiple-pixel output. The term "ghost imaging" was coined soon after the initial experiments were reported, to emphasize that neither of the photocurrents alone yields a target image: the light hitting the bucket detector has interacted with the target, but that detector has no spatial resolution, whereas the light hitting the multipixel detector has not interrogated the target. However, cross correlating the two photocurrents does produce a target image. Figure 1 shows the generic lensless ghost-imaging configuration that will be the focus for the sections below.

The brief qualitative description of ghost imaging that we have just given purposefully avoids what, for some, has been a raging question. Is ghost image formation a quantum effect, or is it classical? Providing a definitive answer to that question—which we shall do in what follows—requires a careful and explicit definition for what constitutes a quantum as opposed to a classical effect within the Fig. 1 construct. At its heart will be the distinction between classical-state and nonclassical-state light beams that we will present in Section 2. Ultimately, we will see that both type light beams are viable sources for ghost imaging. The choice between the two, however, does affect the spatial resolution, field of view, contrast, and signal-to-noise ratio (SNR) of the resulting ghost image.

Work on ghost imaging has resulted in a long list of publications that run the gamut from reports of its experimental realizations, to discussions of its fundamental physics, to attempts at distinguishing its classical and quantum features, to suggestions for implementation variations dictated by practical considerations. Let us begin our review by summarizing the major milestones that have been achieved. The first experimental demonstration of ghost imaging, reported in 1995 by Pittman *et al.* [1], utilized the orthogonally polarized signal and idler beams produced by type-II phase-matched spontaneous parametric downconversion (SPDC). These beams—comprising a low-flux stream of frequency-

Figure 1

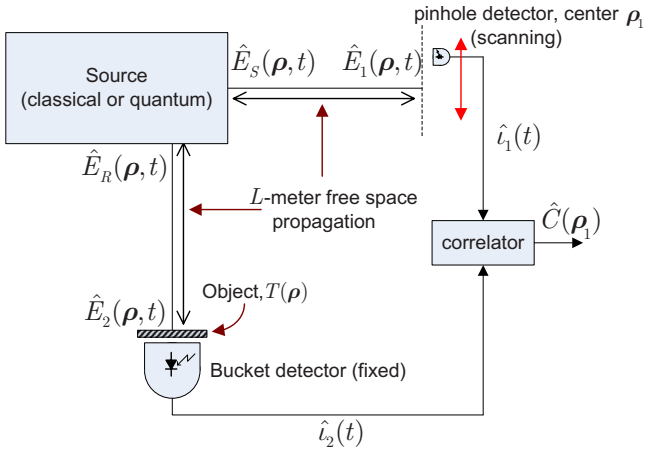

Simple ghost-imaging setup. Correlated signal (S) and reference (R) fields—here shown as quantum operators that can be used to analyze all source possibilities—propagate through L-meter-long free space paths. The signal then illuminates a high-spatial-resolution detector, shown here as a scanning pinhole detector, whereas the reference illuminates a single-pixel (bucket) detector through an object transparency with field transmission $T(\boldsymbol{\rho})$. Cross correlation of the resulting photocurrents yields the ghost image of the intensity transmission $|T(\boldsymbol{\rho})|^2$ as the pinhole is scanned.

entangled signal–idler photon pairs (biphotons)—were separated by a polarizing beam splitter and used as the signal and reference in a ghost-imaging arrangement akin to that shown in Fig. 1. Because of the low-flux nature of the SPDC source, photon-coincidence counting was performed instead of photocurrent cross correlation. The ghost image that Pittman *et al.* obtained was claimed to be a quantum effect, because an entangled-state light source was employed in its generation. In 2002, however, Bennink *et al.* [2] published results from a ghost-imaging-like experiment that used scanning of a pair of collimated laser beams with anticorrelated propagation directions. That the Bennink *et al.* experiment did not rely on entanglement—and that hence its ghost image could be regarded as a classical effect—sparked a debate [3–5] whose prevailing conclusion was that the product of the near-field and far-field spatial resolutions of the images generated by a particular configuration of the classical scheme was inferior to that obtained from a biphoton-state ghost imager. It soon became apparent that this conclusion did not apply universally to all classical-source ghost imagers. Indeed, the similarity between the propagation behavior of the biphoton wave function and the mutual coherence function of thermal radiation [6–8] prompted theoretical analysis of ghost imaging with partially coherent thermal light [9–12], which predicted that ghost images with features qualitatively comparable with the biphoton imager could be achieved. Subsequent experimental demonstrations confirmed this theoretical prediction [13,14]. These experiments were performed with pseudothermal light generated by passing a laser beam through a rotating ground-glass diffuser. The diffusely scattered, time-varying optical field at the output of the ground glass impinged on a 50:50 beam splitter whose output beams provided the signal and reference light for a lensless ghost-imaging arrangement. Because the pseudothermal source could be easily made

dim or bright, it was possible to utilize photon-counting detectors [13] in the former case and a CCD array in the latter [14]. Both the theoretical analysis and the experimental results showed that the main difference between pseudothermal-source ghost images and biphoton-state ghost images was the presence of a very significant featureless background level in the pseudothermal ghost image, something that was not present in the biphoton ghost image.

The discovery that ghost imaging could be performed with bright pseudothermal sources opened the door to a new debate regarding the physics of ghost imaging. Scarcelli *et al.* [15] asserted that thermal-state ghost imaging did *not* admit of a classical interpretation based on the correlation of the intensity fluctuations in the two source beams. Despite several prior articles having successfully used coherence theory [9,10] and classical statistical optics [11,12] to analyze thermal-state ghost imaging and to accurately predict experimental observations, Scarcelli *et al.* argued that a quantum-mechanical description based on nonlocal two-photon interference was compulsory for a quantitatively correct description of thermal-light ghost imaging. Later, however, a conceptual single-beam analysis, employing classical coherence theory, showed that the pseudothermal ghost image resulted from speckle correlation [16], but it did not provide a quantitative comparison between the pseudothermal and biphoton cases. To obtain that missing quantitative comparison, we introduced a unifying Gaussian-state framework [17] that encompassed ghost images formed from pseudothermal and biphoton light, as well as ghost images realized with classical phase-sensitive light. We showed that the point-spread function in biphoton-state ghost imaging depended on the phase-sensitive cross correlation between the two SPDC output fields, whereas in thermal-state ghost imaging the point-spread function depended on their phase-insensitive cross correlation. The fact that a two-field classical Gaussian-state source could, in principle, be engineered to have arbitrary phase-sensitive and phase-insensitive cross correlation functions led us to conclude that ghost image formation with biphoton light was *not* due to quantum entanglement *per se*, but rather to classical coherence propagation. We also showed that the intensity fluctuation interpretation for thermal-state ghost imaging did yield correct quantitative predictions, because the predictions of the semiclassical and quantum theories of photodetection coincide when the incident optical fields are statistical mixtures of coherent states. The idea of using classical phase-sensitive light for ghost imaging, which we originated in [17], was an essential ingredient in our treatment of ghost imaging because it is the two-field classical state that most closely mimics the coherence properties of the biphoton state.

The speckle-correlation interpretation of thermal-state ghost imaging led one of us to the realization that the light-beam behavior that it requires may be obtained by allowing a spatially coherent laser beam to illuminate a spatial light modulator (SLM) whose pixels are driven by statistically independent noise processes [18]. From there it was simple to argue that noise modulation was unnecessary in that driving the pixels with orthogonal or pseudorandom time functions would suffice. Once the realm of deterministic modulation was entered, it became clear that there was no need for the light beam that illuminated the high-spatial-resolution detector, because its illumination was subject only to free-space diffraction and hence could be precomputed from the known drives applied to the SLM. What results is computational ghost imaging: the photocurrent generated by the single-pixel (bucket) detector, as a result of the SLM output light interacting with the target and impinging on the detector, is correlated with the precom-

puted intensity pattern to produce the ghost image. A proof-of-principle experiment for computational ghost imaging was quickly accomplished [19]. Since then, techniques from compressed sensing have been employed to increase the efficiency of computational ghost-image formation, i.e., to reduce the integration time required in order to obtain an image of adequate quality [20].

Although understanding the noise characteristics of ghost imaging is a vital component for assessing its imaging performance, relatively little rigorous SNR analysis had been done for the Fig. 1 configuration until recently. An initial SNR assessment of pseudothermal ghost imaging stated that the SNR should be proportional to the contrast of the image [21]. In other work, the SNRs of classical and quantum ghost imaging (along with other photon-correlation imagers) were reported [22]. There it was shown that at equal photon numbers the SNR of biphoton-state ghost imaging exceeds that of thermal-state ghost imaging. However, in general the higher-SNR-yielding source depends on the particular parameter values. The SNR of biphoton-state ghost imaging was also analyzed in [23], where a trade-off between image resolution and SNR was exhibited. In [24] we extended our unifying Gaussian-state framework from [17] to provide a rigorous SNR analysis for both classical and quantum ghost imaging in the narrowband and broadband limits, and at all brightness levels. Our effort indeed yielded an SNR proportional to the image contrast for bright thermal-state ghost imaging. Furthermore, the biphoton-state ghost imaging SNR was shown to be proportional to the mean coincidence rate. Perhaps most interesting, however, was that the Gaussian-state framework facilitated the first analytic derivation of the full quantum-to-classical transition in SNR, as the brightness of the source fields (from SPDC) transitioned from having much less than one photon per mode to having many photons per mode. Finally, in agreement with the earlier conclusions from [22], the work in [24] showed that neither source (thermal-state or biphoton-state) universally dominates the other: the specific operating parameters, such as bandwidth and source brightness, determine whether classical or quantum sources have superior SNR performance.

The history we have summarized displays the path that will be taken in what follows, viz., a quantitative treatment—relying on Gaussian-state analysis—that proceeds from quantum ghost imaging to classical ghost imaging to computational ghost imaging. Before embarking on that journey, let us note some of the recent advances in ghost imaging that will not be covered. Ghost imaging using homodyne reception, instead of direct detection, has been proposed, and its performance has been analyzed in detail [25]. In this configuration a second-order field moment is measured, rather than a fourth-order moment, so that both phase and amplitude information can be obtained. Fourier-plane ghost imaging of pure-phase objects using biphoton-state sources has been analyzed [26]. Ghost imaging with thermal light has been a major area of interest. Lensless ghost imaging with true thermal light obtained from a hollow cathode lamp has been demonstrated [27], Fourier-plane imaging of pure phase objects has been carried out [28,29], and the transfer functions for lensless ghost-imaging configurations with pointlike detectors in both arms have been analyzed [30]. The possibility of using ghost imaging in remote sensing has led to an experiment that images a target in reflection, rather than the more usual case of imaging in transmission [31,32], and some analysis of ghost imaging through atmospheric turbulence has been reported [33]. A unified theoretical framework, based on statistical optics, has been applied to the Hanbury-Brown Twiss correlation experiment and to thermal-state ghost imaging, showing that in both cases the correlation in inten-

sity fluctuations accurately predicts the experimental observations [34]. Another avenue of recent interest has been to utilize different wavelengths in each arm [35,36]. This approach facilitates the tailoring of the wavelengths in each arm of the ghost imager to optimize imaging efficiency. Ghost-imaging schemes that rely on field moments of higher than fourth order have also been analyzed [37–39] and experimentally demonstrated [40,41].

Our goal is to provide a comprehensive review of the fundamentals of ghost imaging, using (classical and quantum) Gaussian states as the framework for analysis and comparison. Restricting our attention to Gaussian states may seem arbitrary, but such is not the case. The two sources of primary interest to ghost imaging are thermal-state light and biphoton light, which are classical and quantum, respectively, in the sense to be defined in Section 2. The former is obtained by 50:50 beam splitting of a true thermal source (e.g., the hollow cathode lamp of [27]) or a pseudothermal source (laser illumination of a rotating ground-glass diffuser). The latter is the post-selected result of using the signal and idler outputs from SPDC in that source's typical low-brightness, low-flux operating regime. Thermal sources emit zero-mean, Gaussian-distributed mixtures of coherent states. In the absence of pump depletion, the signal and idler obtained from SPDC are in a zero-mean, jointly Gaussian state. Thus, by analyzing classical and quantum ghost imaging within the same Gaussian-state framework, we shall be able to unambiguously identify the features of ghost imaging that contain a true quantum signature. An accompanying benefit to using Gaussian states stems from their analytic convenience. Zero-mean Gaussian states are completely characterized by their correlation functions [42]. Furthermore, because linear transformations (such as free-space diffraction) of Gaussian-state light beams yield Gaussian-state light beams, the output state can be obtained by simply propagating the input field's correlation functions through the same linear system. The convenience afforded by having the state completely characterized by correlation functions is particularly crucial to deriving tractable SNRs, for which the variance of the ghost-image estimate is needed. In short, the unifying Gaussian-state framework developed in this paper is well-suited to developing a physical understanding of ghost imaging and a quantitative treatment of its performance.

The rest of this review article is organized as follows. We begin, in Section 2, by establishing exactly what we mean by "classical" and "quantum" light sources, so as to preclude any ambiguity in our treatment or conclusions. Next, in Section 3, we derive the ghost image signature obtained with general zero-mean Gaussian states and identify phase-sensitive and phase-insensitive cross correlations as the entities facilitating ghost-image formation. Motivated by that identification, we devote Section 4 to the coherence theory for these two correlation classes. In Section 5 we use the results from the previous sections to derive the far-field ghost image signatures of three classes of Gaussian-state sources. First, we consider a source possessing the maximum phase-insensitive cross correlation—as constrained by its autocorrelation functions—but no phase-sensitive cross correlation. Such a source always produces a classical state, and thermal light is of this class. Second, we consider a source with the maximum classical phase-sensitive cross correlation—again constrained by its autocorrelation functions—but no phase-insensitive cross correlation. Finally, we treat the latter source when its phase-sensitive cross correlation is the maximum permitted by quantum mechanics. The low-brightness, low-flux limit of this source yields the biphoton state in postselection. Having derived the image signatures,

we use Section 6 to develop the image SNRs obtained with these three sources. We then treat their image acquisition times in Section 7. In Section 8, we explain the physics of computational ghost imaging, which is rooted in the physics of conventional ghost imaging, and then proceed to an analysis of its working principles. We conclude our review in Section 9, with a discussion of the key results that emerge from our analysis.

2. Semiclassical versus Quantum Photodetection

Before we embark on an analysis that aims to distinguish between the "classical" and "quantum" features of ghost imaging, it is imperative that we provide a quantitative definition of these terms. Light is intrinsically quantum mechanical, and its quantized nature has long been observed through high-sensitivity photodetection [43,44]. Therefore, *all* optical imaging phenomena are fundamentally of a quantum mechanical nature. However, it has long been known [44–48] that the photodetection statistics of a light beam in a coherent state, or a statistical mixture of coherent states, can be *calculated* by using the semiclassical (shot-noise) theory of photodetection. In this theory electromagnetic fields are (possibly random) space–time functions that obey Maxwell's equations, and the fundamental noise in photodetection arises from the discreteness of the electron charge. Despite these two theories' having disparate interpretations for the physical nature of the noise seen in photodetection, the *quantitative* outcome of either calculation is identical when the illuminating quantum field is in a coherent state or a random mixture of coherent states. Therefore, it has been widely accepted that optical phenomena that can be explained with the semiclassical theory do *not* demonstrate the quantum nature of light [44,47,48]. Consequently, throughout this paper we adopt the following conventions: (1) a light beam for which the semiclassical theory of photodetection is valid, i.e., when its predictions coincide with those of the quantum theory, will be said to be in a classical state; and (2) a feature of ghost imaging will be said to be a quantum signature *if and only if* it cannot be accurately quantified with the semiclassical theory of photodetection.

Let us make the discussion from the previous paragraph explicit by introducing our notation for classical fields and quantum field operators and then exhibiting the associated semiclassical and quantum theories of photodetection. Consider an ideal photodetector, i.e., one with unity quantum efficiency, zero dark current, and infinite electrical bandwidth, whose photocurrent, $i(t)$, registers individual photon detection events instantaneously as current impulses carrying charge q. In semiclassical theory, the scalar [49], quasi-monochromatic, paraxial optical field impinging on the photosensitive surface of the photodetector is a positive-frequency classical electromagnetic wave, denoted $E(\boldsymbol{\rho},t)e^{-i\omega_0 t}$, where $\boldsymbol{\rho}$ is a 2D position vector on the detector's planar photosensitive region and ω_0 is the field's center frequency, so that $E(\boldsymbol{\rho},t)$ is its baseband envelope whose bandwidth, Ω, is much smaller than ω_0. For convenience, we assume that this field is normalized to have the units $\sqrt{\text{photons}/\text{m}^2\text{s}}$. Conditioned on perfect knowledge of the field impinging on the photodetector, we have that $i(t)/q$ is an inhomogeneous Poisson impulse train with rate function [46,50]

$$\mu(t) = \int_{\mathcal{A}} \mathrm{d}\boldsymbol{\rho} |E(\boldsymbol{\rho},t)|^2, \tag{1}$$

where $\mathcal{A}$ is the detector's photosensitive region. Thus, regardless of whether the illuminating field is deterministic or random, the photocurrent is subject to the noise that is inherent in this Poisson process, which yields the well-known shot-noise floor of semiclassical photodetection theory [47,48,51]. Randomness in the illumination is then accounted for by taking $E(\boldsymbol{\rho},t)$ to be a stochastic process, as is done in classical statistical optics [52].

In the quantum theory of photodetection, the classical photocurrent produced by the same ideal photodetector is a stochastic process whose statistics coincide with those of the photon-flux operator measurement scaled by the electron charge [53],

$$\hat{\imath}(t) = q \int_{\mathcal{A}} \mathrm{d}\boldsymbol{\rho} \hat{E}^{\dagger}(\boldsymbol{\rho},t) \hat{E}(\boldsymbol{\rho},t). \tag{2}$$

Here $\hat{E}(\boldsymbol{\rho},t)$ is the quantum-mechanical baseband electric field operator, normalized to have $\sqrt{\text{photons}/\text{m}^2\text{s}}$ units, and † indicates Hermitian conjugation. It follows that the photocurrent statistics are determined by the state of $\hat{E}(\boldsymbol{\rho},t)$, and the shot-noise limit of semiclassical theory can be surpassed by some states, such as amplitude-squeezed states, or the eigenkets of continuous-time photodetection [47,48,51,53,54]. It has long been known [47,48,51,53], however, that when $\hat{E}(\boldsymbol{\rho},t)$ is in the coherent state $|E(\boldsymbol{\rho},t)\rangle$, indexed by its eigenfunction $E(\boldsymbol{\rho},t)$ and satisfying

$$\hat{E}(\boldsymbol{\rho},t)|E(\boldsymbol{\rho},t)\rangle = E(\boldsymbol{\rho},t)|E(\boldsymbol{\rho},t)\rangle, \tag{3}$$

the statistics of the $\hat{\imath}(t)$ measurement are identical to those from the semiclassical theory with the impinging classical field taken to be $E(\boldsymbol{\rho},t)$. More generally, the two photodetection theories yield identical statistics for any quantum state that is a classical statistical mixture of coherent states—viz., for all states that have proper P representations [44]—when the classical field used in the semiclassical theory comprises the same statistical mixture of the coherent-state eigenfunctions [47,48,51,55,56]. Moreover, mixtures of coherent states are the only quantum states for which all quantum photodetection statistics—in particular, those of direct, homodyne, and heterodyne detection [47,48]—coincide with the corresponding results found from the semiclassical theory.

Because the correlation measurement at the heart of ghost imaging is a derived statistic from two photodetection measurements, we conclude that the quantum theory of ghost imaging using source states that have proper P representations will yield results equivalent to the classical theory of ghost imaging using the corresponding (classical) random optical fields plus semiclassical (shot-noise) photodetection theory. Therefore, any truly quantum features of ghost imaging are necessarily exclusive to optical field states that do *not* possess proper P representations.

Having detailed our convention for the using the "classical" and "quantum" nomenclature, we will use the quantum theory for what follows because it is universally valid. The reader is cautioned to remember that whenever a feature is deemed classical, there is a derivation using classical fields and semiclassical photodetection that yields identical answers to what was found from the quantum treatment.

3. Gaussian-State Ghost Imaging

Consider the ghost-imaging configuration shown in Fig. 1. An optical source generates two scalar, quasi-monochromatic, paraxial, positive-frequency optical fields [57], a signal $\hat{E}_S(\boldsymbol{\rho},t)e^{-i\omega_0 t}$ and a reference $\hat{E}_R(\boldsymbol{\rho},t)e^{-i\omega_0 t}$, with $\sqrt{\text{photons}/\text{m}^2\text{s}}$ units and common center frequency ω_0, where $\boldsymbol{\rho}$ is the transverse coordinate with respect to each field's optical axis. The commutation relations for the baseband field operators are given by [53]

$$[\hat{E}_m(\boldsymbol{\rho}_1,t_1),\hat{E}_\ell(\boldsymbol{\rho}_2,t_2)]=0, \tag{4}$$

$$[\hat{E}_m(\boldsymbol{\rho}_1,t_1),\hat{E}_\ell^\dagger(\boldsymbol{\rho}_2,t_2)]=\delta_{m,\ell}\delta(\boldsymbol{\rho}_1-\boldsymbol{\rho}_2)\delta(t_1-t_2), \tag{5}$$

where $\delta_{m,\ell}$ is the Kronecker delta function, $m,\ell=S,R$, and $\delta(\cdot)$ is the unit impulse. Both beams undergo L meters of quasi-monochromatic, paraxial, free-space diffraction along their respective optical axes, yielding the detection-plane field operators [47,48,58]

$$\hat{E}_\ell(\boldsymbol{\rho},t)=\int \mathrm{d}\boldsymbol{\rho}'\hat{E}_m(\boldsymbol{\rho}',t-L/c)h_L(\boldsymbol{\rho}-\boldsymbol{\rho}'), \tag{6}$$

where $(\ell,m)=(1,S)$ or $(\ell,m)=(2,R)$, c is the speed of light, $h_L(\boldsymbol{\rho})$ is the Huygens–Fresnel Green's function,

$$h_L(\boldsymbol{\rho})\equiv\frac{e^{i2\pi L/\lambda_0}e^{i\pi|\boldsymbol{\rho}|^2/\lambda_0 L}}{i\lambda_0 L}, \tag{7}$$

and $\lambda_0=2\pi c/\omega_0$ is the wavelength associated with the center frequency. At the detection planes, $\hat{E}_1(\boldsymbol{\rho},t)$ illuminates a quantum-limited pinhole photodetector of area A_1 whose photosensitive region $\boldsymbol{\rho}\in\mathcal{A}_1$ is centered at the transverse coordinate $\boldsymbol{\rho}_1$, while $\hat{E}_2(\boldsymbol{\rho},t)$ illuminates a field-transmission mask $T(\boldsymbol{\rho})$ located immediately in front of a quantum-limited bucket photodetector with photosensitive region $\boldsymbol{\rho}\in\mathcal{A}_2$. Each photodetector is modeled as the cascade of a transmissivity η attenuator, followed by an ideal photodetector—as described in Section 2—whose photocurrent is then low-pass filtered by a real-valued impulse response $h_B(t)$. Such an arrangement then represents a quantum-efficiency η detector with no dark current, no thermal noise, and finite electrical bandwidth.

The ghost image at the transverse coordinate $\boldsymbol{\rho}_1$ is formed by time-averaging the product of the detector photocurrents, which is equivalent to a measurement of the quantum operator

$$\hat{C}(\boldsymbol{\rho}_1)=\frac{1}{T_I}\int_{-T_I/2}^{T_I/2}\mathrm{d}t\hat{\imath}_1(t)\hat{\imath}_2(t), \tag{8}$$

where

$$\hat{\imath}_m(t)=q\int \mathrm{d}u\int_{\mathcal{A}_m}\mathrm{d}\boldsymbol{\rho}\hat{E}_m'^\dagger(\boldsymbol{\rho},u)\hat{E}_m'(\boldsymbol{\rho},u)h_B(t-u), \tag{9}$$

for $m=1,2$, with T_I being the duration of the averaging interval. The field operators appearing in these photocurrent operators are

$$\hat{E}'_m(\boldsymbol{\rho},t) \equiv \begin{cases} \sqrt{\eta}\hat{E}_1(\boldsymbol{\rho},t) + \sqrt{1-\eta}\hat{E}_{\mathrm{vac}_1}(\boldsymbol{\rho},t), & \text{for } m=1, \\ \sqrt{\eta}T(\boldsymbol{\rho})\hat{E}_2(\boldsymbol{\rho},t) + \sqrt{1-\eta|T(\boldsymbol{\rho})|^2}\hat{E}_{\mathrm{vac}_2}(\boldsymbol{\rho},t), & \text{for } m=2, \end{cases} \tag{10}$$

where the $\{\hat{E}_{\mathrm{vac}_m}(\boldsymbol{\rho},t)\}$—which are needed to ensure commutator preservation in accounting for $\eta<1$ photodetection—are in their vacuum states. The $\hat{C}(\boldsymbol{\rho}_1)$ measurement yields an unbiased estimate of the ensemble-average equal-time photocurrent cross-correlation function

$$\begin{aligned} \langle \hat{C}(\boldsymbol{\rho}_1)\rangle &= \langle \hat{i}_1(t)\hat{i}_2(t)\rangle \\ &= q^2\eta^2 A_1 \int_{\mathcal{A}_2} \mathrm{d}\boldsymbol{\rho} \int \mathrm{d}u_1 \int \mathrm{d}u_2 h_B(t-u_1)h_B(t-u_2)|T(\boldsymbol{\rho})|^2 \\ &\quad \times \langle \hat{E}_1^\dagger(\boldsymbol{\rho}_1,u_1)\hat{E}_2^\dagger(\boldsymbol{\rho},u_2)\hat{E}_1(\boldsymbol{\rho}_1,u_1)\hat{E}_2(\boldsymbol{\rho},u_2)\rangle, \end{aligned} \tag{11}$$

where we have approximated the integral over the pinhole detector's photosensitive region as the value of the integrand at $\boldsymbol{\rho}_1$ times the photosensitive area A_1.

The expression in Eq. (11) shows that the ghost image is a linear transformation on the spatial profile of the mask's photon-flux transmissivity, $|T(\boldsymbol{\rho})|^2$. Hence, the point-spread function (impulse response) of this transformation determines the ghost image's behavior, i.e., its field of view and spatial resolution. However, because the point-spread function is determined by a fourth-order moment of $\hat{E}_1$ and $\hat{E}_2$, it is, in general, cumbersome to evaluate. Fortunately, further simplifications are possible when the source state is restricted to be a zero-mean jointly Gaussian state. In particular, because the free-space diffraction integral is a linear transformation, the detection plane field operators $\hat{E}_1$ and $\hat{E}_2$ are in a zero-mean jointly Gaussian state whenever $\hat{E}_S$ and $\hat{E}_R$ are in a zero-mean jointly Gaussian state. Then, using the moment-factoring theorem for Gaussian states (which is a standard recipe for expressing arbitrary moments of Gaussian-state field operators in terms of their second-order moments) [44,59], we can reduce the required fourth-order field moment to the following sum of second-moment products:

$$\begin{aligned} &\langle \hat{E}_1^\dagger(\boldsymbol{\rho}_1,u_1)\hat{E}_2^\dagger(\boldsymbol{\rho},u_2)\hat{E}_1(\boldsymbol{\rho}_1,u_1)\hat{E}_2(\boldsymbol{\rho},u_2)\rangle \\ &\quad = \langle \hat{E}_1^\dagger(\boldsymbol{\rho}_1,u_1)\hat{E}_1(\boldsymbol{\rho}_1,u_1)\rangle\langle \hat{E}_2^\dagger(\boldsymbol{\rho},u_2)\hat{E}_2(\boldsymbol{\rho},u_2)\rangle \\ &\qquad + |\langle \hat{E}_1^\dagger(\boldsymbol{\rho}_1,u_1)\hat{E}_2(\boldsymbol{\rho},u_2)\rangle|^2 + |\langle \hat{E}_1(\boldsymbol{\rho}_1,u_1)\hat{E}_2(\boldsymbol{\rho},u_2)\rangle|^2. \end{aligned} \tag{12}$$

Following the prior literature [51,55], we refer to second-order field moments of the form $\langle \hat{E}_m^\dagger(\boldsymbol{\rho}_1,t_1)\hat{E}_\ell(\boldsymbol{\rho}_2,t_2)\rangle$ as *phase-insensitive* correlation functions (here $m,\ell=1,2$, but in general they can refer to any field index), because only the relative phase between the two fields affects this moment. On the other hand, we call second-order field moments of the form $\langle \hat{E}_m(\boldsymbol{\rho}_1,t_1)\hat{E}_\ell(\boldsymbol{\rho}_2,t_2)\rangle$ *phase-sensitive* correlation functions, because they depend on the fields' absolute phases. For both the phase-insensitive and phase-sensitive correlations the $m=\ell$ cases are *autocorrelation* functions, whereas the $m\neq\ell$ cases are *cross-correlation* functions.

To simplify our analysis, while preserving the essential physics of ghost imaging, let us assume that the baseband signal and reference fields are cross-spectrally pure, complex stationary, and that their phase-sensitive autocorrelation functions are zero, i.e.,

$$\langle \hat{E}_m^\dagger(\boldsymbol{\rho}_1,t_1)\hat{E}_\ell(\boldsymbol{\rho}_2,t_2)\rangle = K_{m,\ell}^{(n)}(\boldsymbol{\rho}_1,\boldsymbol{\rho}_2)\mathcal{R}_{m,\ell}^{(n)}(t_2-t_1), \tag{13}$$

$$\langle \hat{E}_S(\boldsymbol{\rho}_1,t_1)\hat{E}_R(\boldsymbol{\rho}_2,t_2)\rangle = K_{S,R}^{(p)}(\boldsymbol{\rho}_1,\boldsymbol{\rho}_2)\mathcal{R}_{S,R}^{(p)}(t_2-t_1), \tag{14}$$

$$\langle \hat{E}_m(\boldsymbol{\rho}_1,t_1)\hat{E}_m(\boldsymbol{\rho}_2,t_2)\rangle = 0, \tag{15}$$

for $m,\ell = S,R$. Here the superscripts (n) and (p) label normally ordered (phase-insensitive) and phase-sensitive terms, respectively. For convenience, and with no loss of generality, let us also assume that

$$\mathcal{R}_{m,\ell}^{(n)}(0) = \mathcal{R}_{S,R}^{(p)}(0) = 1. \tag{16}$$

Then, paraxial, quasi-monochromatic diffraction in free space over the L-meter-long propagation paths transform the zero-mean, jointly Gaussian state of the source, with correlation functions given in Eqs. (13)–(15), into a zero-mean, jointly Gaussian state at the detection planes whose correlation functions are cross-spectrally pure and given by

$$\langle \hat{E}_m^\dagger(\boldsymbol{\rho}_1,t_1)\hat{E}_\ell(\boldsymbol{\rho}_2,t_2)\rangle = K_{m,\ell}^{(n)}(\boldsymbol{\rho}_1,\boldsymbol{\rho}_2)\mathcal{R}_{m,\ell}^{(n)}(t_2-t_1), \tag{17}$$

$$\langle \hat{E}_1(\boldsymbol{\rho}_1,t_1)\hat{E}_2(\boldsymbol{\rho}_2,t_2)\rangle = K_{1,2}^{(p)}(\boldsymbol{\rho}_1,\boldsymbol{\rho}_2)\mathcal{R}_{1,2}^{(p)}(t_2-t_1), \tag{18}$$

$$\langle \hat{E}_m(\boldsymbol{\rho}_1,t_1)\hat{E}_m(\boldsymbol{\rho}_2,t_2)\rangle = 0, \tag{19}$$

for $m,\ell = 1,2$. In these expressions,

$$K_{m,\ell}^{(n)}(\boldsymbol{\rho}_1,\boldsymbol{\rho}_2) = \int \mathrm{d}\boldsymbol{\rho}_1' \int \mathrm{d}\boldsymbol{\rho}_2' K_{m',\ell'}^{(n)}(\boldsymbol{\rho}_1',\boldsymbol{\rho}_2') h_L^*(\boldsymbol{\rho}_1-\boldsymbol{\rho}_1') h_L(\boldsymbol{\rho}_2-\boldsymbol{\rho}_2'), \tag{20}$$

$$K_{1,2}^{(p)}(\boldsymbol{\rho}_1,\boldsymbol{\rho}_2) = \int \mathrm{d}\boldsymbol{\rho}_1' \int \mathrm{d}\boldsymbol{\rho}_2' K_{S,R}^{(p)}(\boldsymbol{\rho}_1',\boldsymbol{\rho}_2') h_L(\boldsymbol{\rho}_1-\boldsymbol{\rho}_1') h_L(\boldsymbol{\rho}_2-\boldsymbol{\rho}_2'), \tag{21}$$

for $(m,m') = (1,S)$ or $(m,m') = (2,R)$, and likewise for (ℓ,ℓ'). In addition, because the quasi-monochromatic quantum Huygens–Fresnel principle, Eq. (6), only involves delay in time, the temporal correlation behavior is unaffected by propagation. It follows that the fundamental difference between the propagation of phase-insensitive and phase-sensitive correlation functions is the lack of conjugation in the propagation kernel of the latter. Nonetheless, this difference is responsible for significantly different propagation characteristics, which we will describe in the next section.

Substituting Eq. (12) into Eq. (11), along with Eqs. (17) and (18), simplifies the photocurrent cross-correlation expression to

$$\langle \hat{C}(\boldsymbol{\rho}_1)\rangle = C_0(\boldsymbol{\rho}_1) + \int_{\mathcal{A}_2} \mathrm{d}\boldsymbol{\rho}[C_n|K_{1,2}^{(n)}(\boldsymbol{\rho}_1,\boldsymbol{\rho})|^2 + C_p|K_{1,2}^{(p)}(\boldsymbol{\rho}_1,\boldsymbol{\rho})|^2]|T(\boldsymbol{\rho})|^2, \tag{22}$$

where

$$C_0(\boldsymbol{\rho}_1) = q^2\eta^2 A_1\left(\int \mathrm{d}t h_B(t)\right)^2 K_{1,1}^{(n)}(\boldsymbol{\rho}_1,\boldsymbol{\rho}_1)\int_{\mathcal{A}_2}\mathrm{d}\boldsymbol{\rho}K_{2,2}^{(n)}(\boldsymbol{\rho},\boldsymbol{\rho})|T(\boldsymbol{\rho})|^2 \tag{23}$$

is a nonnegative, non-image-bearing background [60] and

$$C_n = q^2\eta^2 A_1[|\mathcal{R}_{1,2}^{(n)}(t)|^2 \star h_B(t)\star h_B(-t)]_{t=0}, \tag{24}$$

$$C_p = q^2\eta^2 A_1[|\mathcal{R}_{1,2}^{(p)}(t)|^2 \star h_B(t)\star h_B(-t)]_{t=0} \tag{25}$$

are constants that depend on the temporal cross correlations between $\hat{E}_1$ and $\hat{E}_2$, the parameters of the photodetectors, and the electron charge q [61].

We therefore conclude that the ghost image, defined as the image-bearing term in $\langle \hat{C}(\boldsymbol{\rho}_1)\rangle$, is equal to the target's intensity transmission profile, $|T(\boldsymbol{\rho})|^2$, filtered through a linear, space-varying point-spread function. For a ghost image obtained with zero-mean Gaussian-state light, this point-spread function is equal to the weighted sum of the squared magnitudes of the phase-insensitive and phase-sensitive cross-correlation functions at the planes of detection in the signal and reference arms of the imager.

4. Phase-Insensitive versus Phase-Sensitive Coherence

Equation (22) shows that, in general, *both* the phase-insensitive and phase-sensitive cross-correlation functions of the detection-plane field operators contribute to the ghost image's point-spread function. As we shall see in the next section, the phase-sensitive cross correlation vanishes in thermal-state ghost imaging, so that its point-spread function depends only on the phase-insensitive cross correlation. Conversely, in biphoton-state ghost imaging and in classical phase-sensitive-light ghost imaging the phase-insensitive cross correlation is zero, and the point-spread function depends only on the phase-sensitive cross correlation. Therefore it is critical that we understand the physics implied by these two types of coherence. Developing that understanding is the goal in the present section.

Although the difference between the phase-insensitive and phase-sensitive correlation functions is only the conjugation of one of the field operators in the former, the physical consequences are profound. In order to develop a crisp analytic understanding of the distinctions, we assume that the cross-spectrally pure correlation functions we have introduced in (13)–(15) have a Gaussian form; namely, they are Gaussian–Schell model correlation functions [44,52,62]. Because the propagation paths in the two arms of the ghost imager are identical, the distinction between cross-correlation propagation and autocorrelation propagation is inconsequential. So, to simplify the physical descriptions in this section, and with no loss in generality, we shall focus on autocorrelation functions.

First, suppose that the phase-insensitive correlation function is given by

$$\langle \hat{E}^{\dagger}(\boldsymbol{\rho}_1,t_1)\hat{E}(\boldsymbol{\rho}_2,t_2)\rangle = \frac{2P}{\pi a_0^2} e^{-(|\boldsymbol{\rho}_1|^2+|\boldsymbol{\rho}_2|^2)/a_0^2 - |\boldsymbol{\rho}_2-\boldsymbol{\rho}_1|^2/2\rho_0^2} e^{-(t_2-t_1)^2/2T_0^2}, \quad (26)$$

where P denotes the photon flux; a_0 is the beam radius (defined as the radius at which the photon irradiance profile is attenuated by e^{-2} relative to the peak beam irradiance); ρ_0 is the coherence radius, which is assumed to satisfy the low-coherence condition $\rho_0 \ll a_0$; and T_0 is the coherence time. The physics immediately apparent from this expression is that the phase-insensitive fluctuations observed at the space–time coordinates $(\boldsymbol{\rho}_1,t_1)$ and $(\boldsymbol{\rho}_2,t_2)$ are correlated when $\boldsymbol{\rho}_1$ and $\boldsymbol{\rho}_2$ are separated by a distance smaller than the coherence length ρ_0, while both are within the beam radius a_0, and when t_1 and t_2 are separated by less than the coherence time T_0. Additional insight can be obtained in the frequency domain by writing the baseband field operator in terms of its monochromatic plane-wave components, i.e., as

$$\hat{E}(\boldsymbol{\rho},t) = \int_{\mathbb{R}^2} \frac{\mathrm{d}\mathbf{k}}{2\pi} \int_{-\infty}^{\infty} \frac{\mathrm{d}\Omega}{\sqrt{2\pi}} \hat{A}(\mathbf{k},\Omega) e^{i\mathbf{k}\cdot\boldsymbol{\rho}-i\Omega t}, \quad (27)$$

where $\mathbf{k}$ is the transverse spatial-frequency vector and Ω is the temporal frequency [62]. In this expression $\hat{A}(\mathbf{k},\Omega)$ is a frequency-domain operator satisfying the canonical commutation relations

$$[\hat{A}(\mathbf{k}_1,\Omega_1),\hat{A}(\mathbf{k}_2,\Omega_2)] = 0, \quad (28)$$

$$[\hat{A}(\mathbf{k}_1,\Omega_1),\hat{A}^{\dagger}(\mathbf{k}_2,\Omega_2)] = \delta(\mathbf{k}_1-\mathbf{k}_2)\,\delta(\Omega_1-\Omega_2). \quad (29)$$

Because of the quasi-monochromatic paraxial approximation we made earlier, $\hat{A}(\mathbf{k},\Omega)$ is excited (i.e., not in a vacuum state) only for $|\mathbf{k}| \ll \omega_0/c$ and $|\Omega| \ll \omega_0$.

Applying the inverse transform associated with Eq. (27) to the phase-insensitive correlation function in Eq. (26), we obtain

$$\langle \hat{A}^{\dagger}(\mathbf{k}_1,\Omega_1)\hat{A}(\mathbf{k}_2,\Omega_2)\rangle = \frac{PT_0\rho_0^2}{\sqrt{2\pi}} e^{-a_0^2|\mathbf{k}_d|^2/8-\rho_0^2|\mathbf{k}_s|^2/2} e^{-T_0^2\Omega_2^2/2}\delta(\Omega_2-\Omega_1), \quad (30)$$

where $\mathbf{k}_s \equiv (\mathbf{k}_1+\mathbf{k}_2)/2$ and $\mathbf{k}_d \equiv \mathbf{k}_2-\mathbf{k}_1$, and we have used the low-coherence condition to write $1/a_0^2+1/\rho_0^2 \approx 1/\rho_0^2$. As shown in Fig. 2(a), this correlation function implies that the angular extent of the source radiation (found by setting $\mathbf{k}_d=\mathbf{0}$) is $2\lambda_0/\pi\rho_0$ and that the angular extent of the source coherence (found by setting $\mathbf{k}_s=\mathbf{0}$) is $2\lambda_0/\pi a_0$. Furthermore, the source bandwidth is given by $2/T_0$ and distinct-frequency plane-wave components of the source are uncorrelated. In words, phase-insensitive coherence is both *monochromatic* and *quasi-monoplanatic*. The former feature is evident from the delta-function temporal-frequency term in Eq (30). To better understand the latter, consider the plane-wave components at a given detuning, Ω. They have significant excitation only within the source's radiation cone, which has full cone angle $2\lambda_0/\pi\rho_0$. More important, these plane-wave components are only correlated with neighboring frequency-Ω plane-wave components that lie within the source's coherence cone, whose cone angle, $2\lambda_0/\pi a_0$, is much smaller than that of the radiation

Figure 2

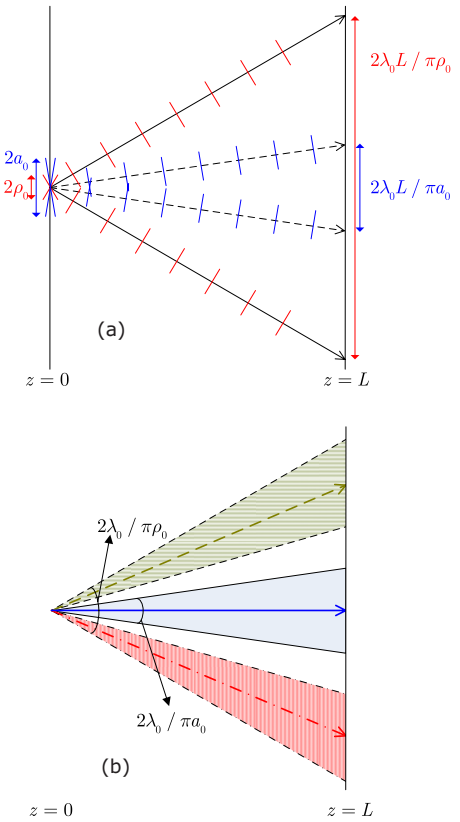

Coherence behavior and angular spectrum of the source-plane ($z=0$) baseband field operator $\hat{E}(\boldsymbol{\rho},t)$ with *phase-insensitive* correlation function given by Eq. (26). (a) The average $z=L$ plane irradiance is appreciable only within a region of diameter $2\lambda_0 L/\pi\rho_0$ (red) around the optical axis. The phase-insensitive fluctuations seen at two transverse points that are symmetrically displaced from the optical axis are correlated only when their separation is less than $2\lambda_0 L/\pi a_0$ (blue). (b) Three plane-wave components are shown here as three arrows with different colors (and line styles). The plane waves (of the same frequency) with which they have phase-insensitive correlation lie within the shaded cones of the same color (and same line-style borders). Because phase-insensitive coherence is quasi-monoplanatic, the coherence cone for each plane wave is centered on its own propagation direction.

cone. This spatial-coherence behavior of the phase-insensitive correlation is illustrated in Fig. 2(b).

The phase-insensitive coherence behavior that we have just reviewed is well known [44]. We have provided its detailed description for comparison with the behavior of *phase-sensitive* coherence that, although it has received much less attention [63], plays a key role in quantum ghost imaging. To parallel our development for the phase-insensitive case, we now suppose that the phase-sensitive correlation function is given by the same Gaussian–Schell model, i.e.,

$$\langle \hat{E}(\boldsymbol{\rho}_1,t_1)\hat{E}(\boldsymbol{\rho}_2,t_2)\rangle = \frac{2P_s}{\pi a_0^2} e^{-(|\boldsymbol{\rho}_1|^2+|\boldsymbol{\rho}_2|^2)/a_0^2} e^{-|\boldsymbol{\rho}_2-\boldsymbol{\rho}_1|^2/2\rho_0^2} e^{-(t_2-t_1)^2/2T_0^2}, \tag{31}$$

where

$$P_s \equiv \int_{\mathbb{R}^2} \mathrm{d}\boldsymbol{\rho}\langle \hat{E}^2(\boldsymbol{\rho},t)\rangle \tag{32}$$

is the mean-squared phase-sensitive flux, and a_0, $\rho_0 \ll a_0$, and T_0 are now, respectively, the radius of mean-squared phase-sensitive excitation, the coherence length, and the coherence time of that excitation. Consequently, $\hat{E}(\boldsymbol{\rho}_1,t_1)$ and $\hat{E}(\boldsymbol{\rho}_2,t_2)$ have appreciable phase-sensitive correlation when $\boldsymbol{\rho}_1$ and $\boldsymbol{\rho}_2$ are both within the phase-sensitive excitation radius a_0, have spatial separation less than the coherence length ρ_0, and temporal separation less than the coherence time T_0. Except for this source-plane description involving phase-sensitive correlation, rather than phase-insensitive correlation, it is unchanged from what we saw in conjunction with Eq. (26). The angular spectrum associated with the phase-sensitive correlation, however, reveals a rather different and quite interesting picture, as we will now show.

Applying the inverse transform associated with Eq. (27) to Eq. (31), we obtain

$$\langle \hat{A}(\mathbf{k}_1,\Omega_1)\hat{A}(\mathbf{k}_2,\Omega_2)\rangle = \frac{P_s T_0 \rho_0^2}{\sqrt{2\pi}} e^{-a_0^2|\mathbf{k}_s|^2/2} e^{-\rho_0^2|\mathbf{k}_d|^2/8} e^{-T_0^2\Omega_2^2/2}\delta(\Omega_2+\Omega_1), \tag{33}$$

where $\mathbf{k}_s \equiv (\mathbf{k}_1+\mathbf{k}_2)/2$ and $\mathbf{k}_d \equiv \mathbf{k}_2-\mathbf{k}_1$ as before, and we have again used the low-coherence $1/a_0^2+1/\rho_0^2 \approx 1/\rho_0^2$ approximation. Thus, as illustrated in Fig. 3(a), the angular extent of phase-sensitive excitation (found by setting $\mathbf{k}_d=\mathbf{0}$) is $2\lambda_0/\pi a_0$, and the angular extent of the phase-sensitive correlation (found by setting $\mathbf{k}_s=\mathbf{0}$), is given by $2\lambda_0/\pi\rho_0$. The source bandwidth is $2/T_0$, and plane-wave pairs with antipodal detunings within this bandwidth have nonzero phase-sensitive cross correlation, but all other frequency pairs are uncorrelated. It follows that phase-sensitive light is *bichromatic* and *quasi-biplanatic*. The former feature is due to the delta-function temporal-frequency term in Eq. (33). To better appreciate the latter, consider the plane-wave components at $\pm(\mathbf{k},\Omega)$. Each has appreciable phase-sensitive flux only when $\theta \equiv \lambda_0|\mathbf{k}|/2\pi$ lies within the source phase-sensitive radiation cone, which has full cone angle $2\lambda_0/\pi\rho_0$. More important, the $(\mathbf{k},\Omega)$ plane-wave component has phase-sensitive cross correlation only with the frequency $-\Omega$ plane-wave components whose spatial frequencies lie within its coherence cone, which is centered at $-\theta$ in angle ($-\mathbf{k}$ in spatial frequency) and has cone angle $2\lambda_0/\pi a_0$. This spatial coherence structure of phase-sensitive correlation is illustrated in Fig. 3(b). Thus, although we have started with identical correlation functions for the two coherence classes, we have found that the physics implied by the two classes of coherence is notably different. That difference will be further explored below, where we examine far-field propagation of our phase-insensitive and phase-sensitive Gaussian–Schell model correlation functions, and in the upcoming sections, where we will see that the difference in the physics results in some distinct ghost-image characteristics. Before doing so, however, some additional comments are in order.

We have noted that there is very little that has been published on the coherence theory for phase-sensitive light; see [44], where it is not even mentioned. Yet bichromatic, biplanatic light-wave behavior figures prominently in a context of

Figure 3

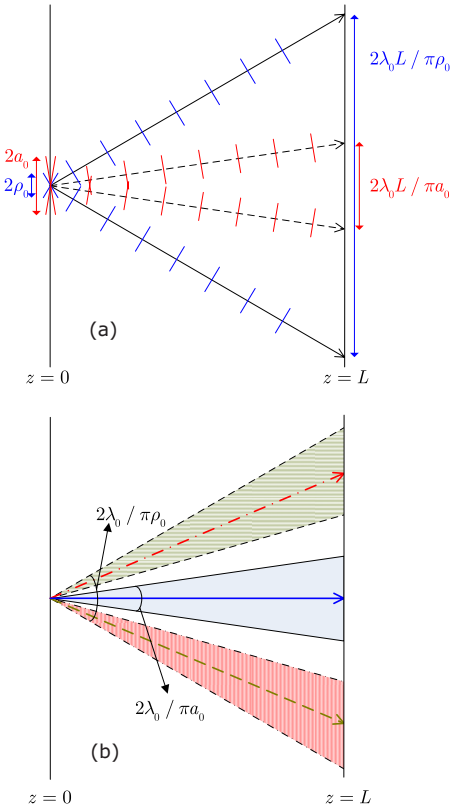

Coherence behavior and angular spectrum of the source-plane ($z=0$) baseband field operator $\hat{E}(\boldsymbol{\rho},t)$ with the *phase-sensitive* correlation function given in Eq. (31). (a) The mean-square phase-sensitive fluctuations on the $z=L$ plane are appreciable within the diameter $2\lambda_0 L/\pi a_0$ (red). The phase-sensitive fluctuations seen at two transverse points displaced in the opposite direction by an equal amount are correlated as long as the distance between the two points is less than $2\lambda_0 L/\pi\rho_0$ (blue). (b) Three plane-wave components are shown here as three arrows with different colors (and line styles). The plane waves with which they have phase-sensitive correlation are shown as shaded cones having the same color (and same line-style borders). Because phase-sensitive coherence is quasi-biplanatic, the coherence cone for each plane wave component is centered around its mirror image about the optical axis.

importance to ghost imaging, namely, the signal and idler beams obtained from continuous-wave (cw), frequency-degenerate SPDC. SPDC with a $+z$-propagating, plane-wave, cw pump can be regarded as a photon-fission process in which a single pump photon at frequency ω_P can split into a signal–idler pair whose frequencies, ω_S and ω_I, obey $\omega_S+\omega_I=\omega_P$, and whose wave vectors, $\mathbf{k}_S$ and $\mathbf{k}_I$, satisfy the phase-matching condition $\mathbf{k}_S+\mathbf{k}_I=k_P\mathbf{i}_z$, where k_P is the pump wave number and $\mathbf{i}_z$ is the z-directed unit vector. As a result, the signal and idler photons in such a pair have frequencies that are bichromatic about $\omega_P/2$, and their transverse wave vectors are antipodal, making these photons biplanatic. Thus, the standard perturbative derivation of the state produced by SPDC leads to a biphoton wave function, for a signal–idler pair, that propagates exactly as does the phase-sensitive cross correlation; see [6] and Eq. (21).

Herein, we assert, lies the root of much confusion about what is classical and what is quantum in ghost imaging. Those characteristics of ghost-image formation that depend on how phase-sensitive cross correlation behaves can be seen with classical-state light. It is *only* those features of ghost imaging that require stronger-than-classical phase-sensitive cross correlation that are intrinsically quantum effects.

We conclude our treatment of coherence theory by describing the far-field, quasi-monochromatic, paraxial propagation of the phase-insensitive and phase-sensitive correlation functions. For this discussion let $\hat{E}_L(\boldsymbol{\rho},t)$ denote the field operator resulting from propagation of $\hat{E}(\boldsymbol{\rho},t)$ over an L-meter-long free-space path. For phase-insensitive coherence propagation, it is well known that a single Fresnel number, $D_0=\pi\rho_0 a_0/\lambda_0 L$, distinguishes between the $D_0\gg 1$ near-field regime—in which diffraction effects are negligible—and the $D_0\ll 1$ far-field regime—in which diffraction spread is dominant [44,52]. Note that this Fresnel number differs from that for the diffraction of a coherent laser beam with intensity radius a_0, which is $D_{\mathrm{coh}}=\pi a_0^2/\lambda_0 L$. This difference reflects the coupling between coherence radius and intensity radius that occurs in free-space diffraction of partially coherent light. The far-field, phase-insensitive correlation function is readily obtained from the source's phase-insensitive angular spectrum, given earlier, by means of the Fraunhofer diffraction integral with the simple substitution of $2\pi\boldsymbol{\rho}/\lambda_0 L$ for $\mathbf{k}$. We find that the far-field phase-insensitive correlation function, stemming from the Gaussian–Schell near-field correlation function of Eq. (26), is

$$\left\langle \hat{E}_L^{\dagger}(\boldsymbol{\rho}_1,t_1)\hat{E}_L(\boldsymbol{\rho}_2,t_2)\right\rangle = \frac{2\pi P\rho_0^2}{\lambda_0^2 L^2} e^{-i\pi(|\boldsymbol{\rho}_1|^2-|\boldsymbol{\rho}_2|^2)/\lambda_0 L} e^{-2\pi^2\rho_0^2|\boldsymbol{\rho}_s|^2/\lambda_0^2 L^2} e^{-\pi^2 a_0^2|\boldsymbol{\rho}_d|^2/2\lambda_0^2 L^2} e^{-(t_2-t_1)^2/2T_0^2}, \tag{34}$$

where $\boldsymbol{\rho}_s=(\boldsymbol{\rho}_1+\boldsymbol{\rho}_2)/2$ and $\boldsymbol{\rho}_d=\boldsymbol{\rho}_2-\boldsymbol{\rho}_1$. This shows that the intensity radius is $a_L=a_0/D_0=\lambda_0 L/\pi\rho_0$ and the coherence radius is given by $\rho_L=\rho_0/D_0=\lambda_0 L/\pi a_0$; i.e., the far-field intensity radius is inversely proportional to its source-plane coherence length, and the far-field coherence length is inversely proportional to the source-plane intensity radius. This behavior is well known from the Van Cittert–Zernike theorem for far-field phase-insensitive coherence propagation [52].

The phase-sensitive correlation function from Eq. (31) propagates in a manner that is distinctly different from its phase-insensitive counterpart. In this case we find that coherence-radius diffraction and mean-square-radius diffraction are decoupled [63]. Two Fresnel numbers are then necessary to distinguish the near field from the far field: the Fresnel number for diffraction of the coherence radius, $D_N=\pi\rho_0^2/\lambda_0 L$, and the Fresnel number for diffraction of the mean-square radius, $D_F=\pi a_0^2/\lambda_0 L$. The near-field regime for phase-sensitive correlation propagation occurs when *both* Fresnel numbers are much greater than one, and the far-field regime is when both are much less than one. Because we have imposed the low-coherence condition, $\rho_0\ll a_0$, we can say that the near-field regime for phase-sensitive coherence propagation is $D_N\gg 1$, and its far-field regime is $D_F\ll 1$. Each of these conditions is more stringent than the corresponding condition for phase-insensitive light. It is easy to compute the far-field form of the Gaussian–Schell model phase-sensitive correlation function from its source's angular spectrum and the Fraunhofer diffraction integral, with the following result:

$$\langle \hat{E}_L(\boldsymbol{\rho}_1,t_1)\hat{E}_L(\boldsymbol{\rho}_2,t_2)\rangle = -\frac{2\pi P_s\rho_0^2}{\lambda_0^2 L^2} e^{i\pi(|\boldsymbol{\rho}_1|^2+|\boldsymbol{\rho}_2|^2)/\lambda_0 L} e^{-2\pi^2 a_T^2|\boldsymbol{\rho}_s|^2/\lambda_0^2 L^2} e^{-\pi^2\rho_0^2|\boldsymbol{\rho}_d|^2/2\lambda_0^2 L^2} e^{-(t_2-t_1)^2/2T_0^2}. \tag{35}$$

Here we have that $\rho_0/D_0=\lambda_0 L/\pi a_0$ is the far-field mean-square radius and $a_0/D_0=\lambda_0 L/\pi\rho_0$ is the far-field coherence radius for the phase-sensitive correlation. Unlike the far-field phase-insensitive case, whose correlation peaks for two points with equal transverse-plane coordinates, the far-field phase-sensitive correlation is highest for two points that are symmetrically disposed about the origin on the transverse plane [6,63], as expected from the quasi-biplanatic nature of the phase-sensitive correlation.

Figure 4 highlights the difference between propagation of the phase-insensitive and phase-sensitive correlation functions. In this figure we have plotted the e^{-2}-attenuation isocontours for the magnitudes of the equal-time source-plane and detection-plane correlation functions in terms of the sum and difference coordinates $\boldsymbol{\rho}_s\equiv(\boldsymbol{\rho}_2+\boldsymbol{\rho}_1)/2$ and $\boldsymbol{\rho}_d\equiv\boldsymbol{\rho}_2-\boldsymbol{\rho}_1$. All transverse-coordinate pairs that correspond to the interior region of a contour are both coherent and intense. It is straightforward to verify that all magnitude isocontours of our Gaussian–Schell model correlations are ellipses. At the source plane, because of our low-coherence assumption, the e^{-2}-attenuation isocontours—for both the phase-insensitive and the phase-sensitive correlation functions—have their minor axes along the difference coordinate. In the far field, we find that diffraction leads to identical increases along the major and minor axes of the phase-insensitive correlation's e^{-2}-attenuation isocontour. For the corresponding far-field phase-

Figure 4

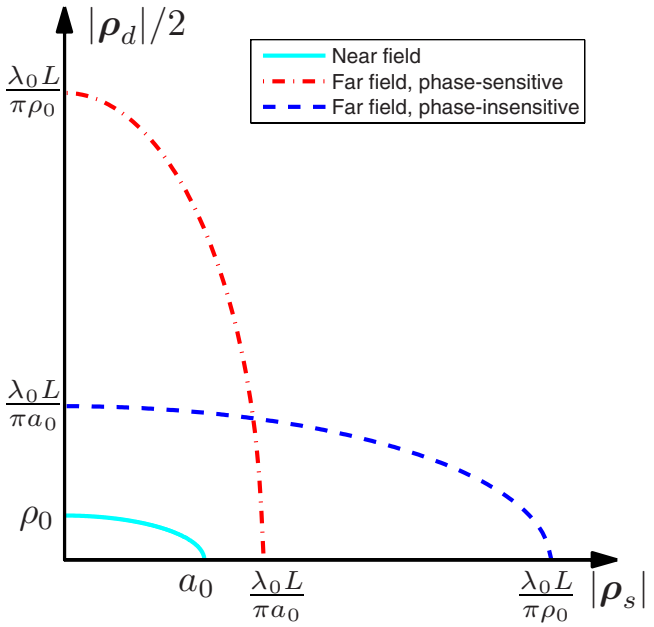

Isocontours corresponding to the e^{-2}-attenuation levels for the phase-sensitive and phase-insensitive correlation functions in the near-field and the far-field regimes.

sensitive correlation's isocontour we get inverted behavior, with its minor axis now aligned with the sum coordinate and its major axis along the difference coordinate. Thus, the far-field phase-insensitive correlation function is dominated by a narrow function in the difference coordinate $|\boldsymbol{\rho}_d|$, whereas the far-field phase-sensitive correlation function is a narrow function in the sum coordinate $|\boldsymbol{\rho}_s|$.

5. Far-Field Ghost Imaging with Quantum and Classical Light

We will now utilize the framework we have developed thus far to derive the far-field ghost images obtained with three different Gaussian-state sources: phase-insensitive light (e.g., pseudothermal or true thermal-state light), classically correlated phase-sensitive light (e.g., two laser beams with phase-conjugate modulations imposed on them), and maximally entangled phase-sensitive light (e.g., the output of ideal SPDC). In all of these cases, we shall assume that the phase-insensitive autocorrelation functions specified in Eq. (13) are the Gaussian–Schell model

$$K_{m,m}^{(n)}(\boldsymbol{\rho}_1,\boldsymbol{\rho}_2)\mathcal{R}_{m,m}^{(n)}(t_2-t_1)=\frac{2P}{\pi a_0^2}e^{-(|\boldsymbol{\rho}_1|^2+|\boldsymbol{\rho}_2|^2)/a_0^2-|\boldsymbol{\rho}_2-\boldsymbol{\rho}_1|^2/2\rho_0^2}e^{-(t_2-t_1)^2/2T_0^2}, \tag{36}$$

for $m=S,R$. Each source will therefore be distinguished by its (phase-insensitive and phase-sensitive) cross-correlation functions, which will be specified in the subsections that follow.

We also assume, for analytic convenience, that the baseband impulse response of the photodetectors, $h_B(t)$, is Gaussian with e^{-2}-attenuation bandwidth Ω_B, i.e.,

$$H_B(\Omega)\equiv\mathcal{F}[h_B(t)]=e^{-2\Omega^2/\Omega_B^2}, \tag{37}$$

where $\mathcal{F}[\cdot]$ denotes the Fourier transform.

5.1. Thermal-State Light

Lensless ghost imaging with thermal-state light usually derives its signal and reference sources from 50:50 beam splitting of a single zero-mean Gaussian-state beam possessing a phase-insensitive autocorrelation function but no phase-sensitive autocorrelation function. Taking the post-splitter signal and reference fields to have the Gaussian–Schell model autocorrelations from Eq. (36), it follows that these fields have the maximum phase-insensitive cross correlation, given by

$$K_{S,R}^{(n)}(\boldsymbol{\rho}_1,\boldsymbol{\rho}_2)R_{S,R}^{(n)}(t_2-t_1)=\frac{2P}{\pi a_0^2}e^{-(|\boldsymbol{\rho}_1|^2+|\boldsymbol{\rho}_2|^2)/a_0^2-|\boldsymbol{\rho}_2-\boldsymbol{\rho}_1|^2/2\rho_0^2}e^{-(t_2-t_1)^2/2T_0^2}, \tag{38}$$

and a vanishing phase-sensitive cross correlation, viz., $K_{S,R}^{(p)}(\boldsymbol{\rho}_1,\boldsymbol{\rho}_2)\mathcal{R}_{S,R}^{(p)}(t_2-t_1)=0$. Because the target is in the far field of the source, i.e., $D_0\ll 1$, we use the propagated source correlations from Section 4, i.e.,

$$|K_{1,2}^{(n)}(\boldsymbol{\rho}_1,\boldsymbol{\rho}_2)\mathcal{R}_{1,2}^{(n)}(t_2-t_1)| = \frac{2P}{\pi a_L^2} e^{-(|\boldsymbol{\rho}_1|^2+|\boldsymbol{\rho}_2|^2)/a_L^2 - |\boldsymbol{\rho}_2-\boldsymbol{\rho}_1|^2/2\rho_L^2} e^{-(t_2-t_1)^2/2T_0^2}, \tag{39}$$

where $a_L = \lambda_0 L/\pi\rho_0$ and $\rho_L = \lambda_0 L/\pi a_0$, and the ghost image signature, from Eq. (22), becomes

$$\langle \hat{C}(\boldsymbol{\rho}_1)\rangle = C_0(\boldsymbol{\rho}_1) + C_n\left(\frac{2P}{\pi a_L^2}\right)^2 e^{-2|\boldsymbol{\rho}_1|^2/a_L^2}\int_{\mathcal{A}_2} \mathrm{d}\boldsymbol{\rho} e^{-|\boldsymbol{\rho}_1-\boldsymbol{\rho}|^2/\rho_L^2} e^{-2|\boldsymbol{\rho}|^2/a_L^2}|T(\boldsymbol{\rho})|^2. \tag{40}$$

Equation (40) reveals three significant features of the far-field thermal-state ghost image. First, the ghost image is space-limited by the reference beam's average intensity profile, so that the object must be placed in the field of view a_L [64]. Second, the useful transverse scanning range of the pinhole detector is restricted to the field of view a_L. Finally, and most important, the finite cross-correlation coherence length ρ_L limits the resolution of the image. When the field-of-view limitations can be neglected, the image signature simplifies to

$$\langle \hat{C}(\boldsymbol{\rho}_1)\rangle = q^2\eta^2 A_1\left(\frac{2P}{\pi a_L^2}\right)^2\left[\int_{\mathcal{A}_2}\mathrm{d}\boldsymbol{\rho}|T(\boldsymbol{\rho})|^2 + \mathcal{C}_t^{(n)}\int_{\mathcal{A}_2}\mathrm{d}\boldsymbol{\rho}e^{-|\boldsymbol{\rho}_1-\boldsymbol{\rho}|^2/\rho_L^2}|T(\boldsymbol{\rho})|^2\right], \tag{41}$$

where $\mathcal{C}_t^{(n)} \equiv 1/\sqrt{1+16/\Omega_B^2 T_0^2}$. So, the ghost image is proportional to the convolution of the object's intensity transmission, $|T(\boldsymbol{\rho})|^2$, with the Gaussian point-spread function $e^{-|\boldsymbol{\rho}|^2/\rho_L^2}$, which limits the spatial resolution, defined here as the radius to the e^{-2} level in the point-spread function, to $\sqrt{2}\rho_L$.

We can use the ghost-image expression from Eq. (41) to calculate the resulting contrast via the following definition:

$$\mathcal{C}^{(n)} \equiv \frac{\max_{\boldsymbol{\rho}_1}[\langle \hat{C}(\boldsymbol{\rho}_1)\rangle] - \min_{\boldsymbol{\rho}_1}[\langle \hat{C}(\boldsymbol{\rho}_1)\rangle]}{C_0(\mathbf{0})}. \tag{42}$$

The numerator in Eq. (42) quantifies the dynamic range of the image-bearing term, while its denominator is the featureless background that is present within the observation region. With this definition we find that this contrast factors as follows:

$$\mathcal{C}^{(n)} = \mathcal{C}_s^{(n)}\mathcal{C}_t^{(n)}, \tag{43}$$

where the temporal (t) factor is defined above, and the spatial (s) factor is given by

$$\mathcal{C}_s^{(n)} = \frac{\max_{\boldsymbol{\rho}_1}[\mathcal{I}_c(\boldsymbol{\rho}_1)] - \min_{\boldsymbol{\rho}_1}[\mathcal{I}_c(\boldsymbol{\rho}_1)]}{\int_{\mathcal{A}_2}\mathrm{d}\boldsymbol{\rho}|T(\boldsymbol{\rho})|^2}, \tag{44}$$

with

$$\mathcal{I}_c(\boldsymbol{\rho}_1) \equiv \int_{\mathcal{A}_2} \mathrm{d}\boldsymbol{\rho} e^{-|\boldsymbol{\rho}_1 - \boldsymbol{\rho}|^2/\rho_L^2} |T(\boldsymbol{\rho})|^2 \tag{45}$$

denoting the point-spread-degraded image of $|T(\boldsymbol{\rho})|^2$. To obtain a closed form contrast expression, we will assume that $T(\boldsymbol{\rho})$ is a binary amplitude mask, as has often been the case in ghost-imaging experiments. It follows that

$$\mathcal{C}_s^{(n)} \approx \pi\rho_L^2/A_T \ll 1, \tag{46}$$

where

$$A_T \equiv \int \mathrm{d}\boldsymbol{\rho} |T(\boldsymbol{\rho})|^2, \tag{47}$$

and the inequality in (46) holds because $A_T/\pi\rho_L^2$ is approximately the number of resolution cells in the ghost image. Combined with the fact that $\mathcal{C}_t^{(n)} \leq 1$, Eq. (46) shows that classical-source ghost imaging *always* has low contrast. This is why thermal-state ghost imaging has been performed with AC coupling of the photocurrents to the correlator [15]. Thermalized laser light is a narrowband source, for which $\Omega_B T_0 \gg 1$ so that $\mathcal{C}_t^{(n)} \approx 1$. The use of AC coupling implies that the correlator is estimating the *cross covariance* between the photocurrents produced by detectors 1 and 2, rather than their cross correlation. This ensemble-average cross covariance is given by $\langle \hat{C}(\boldsymbol{\rho}_1)\rangle - C_0(\boldsymbol{\rho}_1)$; so it might seem that covariance estimation alleviates all concerns with the background term. Such is not the case, as we shall show in the following section. In particular, despite the absence of the background term from the photocurrents' cross covariance, its shot noise and excess noise still affect the image's SNR.

5.2. Classically Correlated Phase-Sensitive Light

Let us now consider a source state that has the maximum phase-sensitive cross correlation permitted by classical physics, given the autocorrelation functions in Eq. (36), but has no phase-insensitive cross correlation, i.e.,

$$K_{S,R}^{(p)}(\boldsymbol{\rho}_1, \boldsymbol{\rho}_2)\mathcal{R}_{S,R}^{(p)}(t_2 - t_1) = \frac{2P}{\pi a_0^2} e^{-(|\boldsymbol{\rho}_1|^2 + |\boldsymbol{\rho}_2|^2)/a_0^2 - |\boldsymbol{\rho}_2 - \boldsymbol{\rho}_1|^2/2\rho_0^2} e^{-(t_2 - t_1)^2/2T_0^2}, \tag{48}$$

and $K_{S,R}^{(n)}(\boldsymbol{\rho}_1, \boldsymbol{\rho}_2)\mathcal{R}_{S,R}^{(n)}(t_2 - t_1) = 0$, where we have assumed the phase-sensitive cross correlation function is real valued. When the source-to-object separation is in the far-field regime for phase-sensitive coherence propagation, i.e., when $D_F \ll 1$ as discussed in Section 4, the source-plane phase-sensitive cross correlation in Eq. (48) gives rise to the following far-field cross-correlation function [63]:

$$|K_{1,2}^{(p)}(\boldsymbol{\rho}_1, \boldsymbol{\rho}_2)\mathcal{R}_{1,2}^{(p)}(t_2 - t_1)| = \frac{2P}{\pi a_L^2} e^{-(|\boldsymbol{\rho}_1|^2 + |\boldsymbol{\rho}_2|^2)/a_L^2 - |\boldsymbol{\rho}_2 + \boldsymbol{\rho}_1|^2/2\rho_L^2} e^{-(t_2 - t_1)^2/2T_0^2}, \tag{49}$$

with a_L and ρ_L as defined above [see below Eq. (39)]. Hence, the ghost image obtained with classical phase-sensitive light is

$$\langle \hat{C}(\boldsymbol{\rho}_1)\rangle = C_0(\boldsymbol{\rho}_1) + C_p\left(\frac{2P}{\pi a_L^2}\right)^2 e^{-2|\boldsymbol{\rho}_1|^2/a_L^2}\int_{\mathcal{A}_2} \mathrm{d}\boldsymbol{\rho} e^{-|\boldsymbol{\rho}_1+\boldsymbol{\rho}|^2/\rho_L^2} e^{-2|\boldsymbol{\rho}|^2/a_L^2}|T(\boldsymbol{\rho})|^2. \tag{50}$$

Once again, we will assume that the region of interest for $T(\boldsymbol{\rho})$ is well within the field of view, i.e., $|\boldsymbol{\rho}| \ll a_L$, so that we can express the ghost image as

$$\langle \hat{C}(\boldsymbol{\rho}_1)\rangle = q^2\eta^2 A_1\left(\frac{2P}{\pi a_L^2}\right)^2\left[\int_{\mathcal{A}_2}\mathrm{d}\boldsymbol{\rho}|T(\boldsymbol{\rho})|^2 + \mathcal{C}_t^{(p)}\int_{\mathcal{A}_2}\mathrm{d}\boldsymbol{\rho}e^{-|\boldsymbol{\rho}_1+\boldsymbol{\rho}|^2/\rho_L^2}|T(\boldsymbol{\rho})|^2\right], \tag{51}$$

where $\mathcal{C}_t^{(p)}=\mathcal{C}_t^{(n)}$ from the previous subsection. Comparing Eq. (51) with Eq. (41), we see that the far-field ghost image formed with classical phase-sensitive light and that formed with phase-insensitive light are identical except that the former is inverted; i.e., the ghost image with phase-sensitive light has field of view a_L and spatial resolution $\sqrt{2}\rho_L$, but the image-bearing term is proportional to $|T(-\boldsymbol{\rho})|^2$ convolved with $e^{-|\boldsymbol{\rho}|^2/\rho_L^2}$. Consequently, ghost imaging with classical phase-sensitive light suffers from the same low contrast as ghost imaging with thermal light, which is given in Eq. (46) for a binary amplitude mask. This could be remedied by use of AC coupling as explained in the previous subsection.

5.3. Maximally Entangled Phase-Sensitive Light

We continue to consider signal and reference beams in a zero-mean jointly Gaussian state with no phase-insensitive cross correlation, but now we take the phase-sensitive cross correlation to be the maximum permitted by *quantum* physics. Because quantum ghost-imaging experiments have used the signal and idler outputs from SPDC for its two source fields, we shall focus on that case here. The output field operators of SPDC can be expressed as [65,66]

$$\hat{E}_m(\boldsymbol{\rho},t) = A(\boldsymbol{\rho})\hat{\mathcal{E}}_m(\boldsymbol{\rho},t) + \hat{\mathcal{L}}_m(\boldsymbol{\rho},t) \tag{52}$$

for $m=S,R$, where $|A(\boldsymbol{\rho})| \le 1$ is an aperture function representing the finite transverse extent of the interaction medium and the $\hat{\mathcal{L}}_m(\boldsymbol{\rho},t)$ are auxiliary vacuum-state operators, so that the $\hat{E}_m(\boldsymbol{\rho},t)$ satisfy the free-space field commutator relations [67]. The operator-valued Fourier transforms of $\{\hat{\mathcal{E}}_m(\boldsymbol{\rho},t), m=S,R\}$, denoted $\{\hat{A}_m(\mathbf{k},\Omega), m=S,R\}$, are given by a two-field Bogoliubov transformation of vacuum-state input field operators, $\hat{a}_m(\mathbf{k},\Omega)$, i.e.,

$$\hat{A}_S(\mathbf{k},\Omega) = \mu(\mathbf{k},\Omega)\hat{a}_S(\mathbf{k},\Omega) + \nu(\mathbf{k},\Omega)\hat{a}_R^\dagger(-\mathbf{k},-\Omega), \tag{53}$$

$$\hat{A}_R(-\mathbf{k},-\Omega) = \mu(\mathbf{k},\Omega)\hat{a}_R(-\mathbf{k},-\Omega) + \nu(\mathbf{k},\Omega)\hat{a}_S^\dagger(\mathbf{k},\Omega). \tag{54}$$

Here $\nu(\mathbf{k},\Omega) \in \mathbb{R}$ and $\mu(\mathbf{k},\Omega) \equiv 1 + i\nu(\mathbf{k},\Omega)$ are the canonical transformation coefficients. In accordance with the Gaussian-Schell model treatment introduced earlier, we set [68]

$$\nu(\mathbf{k},\Omega) = 2(2\pi)^{1/4}\sqrt{\frac{PT_0\rho_0^2}{a_0^2}}e^{-\rho_0^2|\mathbf{k}|^2/4 - T_0^2\Omega^2/4}, \tag{55}$$

$$A(\boldsymbol{\rho}) = \exp\{-|\boldsymbol{\rho}|^2/a_0^2\}, \tag{56}$$

such that the $\hat{E}_m(\boldsymbol{\rho},t)$, for $m=S,R$, are in a zero-mean jointly Gaussian state, with phase-insensitive autocorrelation functions given by Eq. (36), and the maximum permissible phase-sensitive cross-correlation function,

$$\langle \hat{E}_S(\boldsymbol{\rho}_1,t_1)\hat{E}_R(\boldsymbol{\rho}_2,t_2)\rangle = \frac{2P}{\pi a_0^2} e^{-(|\boldsymbol{\rho}_1|^2+|\boldsymbol{\rho}_2|^2)/a_0^2} \times \left[i e^{-|\boldsymbol{\rho}_2-\boldsymbol{\rho}_1|^2/2\rho_0^2} e^{-(t_2-t_1)^2/2T_0^2} + (2/\pi)^{1/4} \sqrt{\frac{a_0^2}{PT_0\rho_0^2}} e^{-|\boldsymbol{\rho}_2-\boldsymbol{\rho}_1|^2/\rho_0^2} e^{-(t_2-t_1)^2/T_0^2} \right]. \tag{57}$$

All other second-order moments, i.e., the phase-sensitive autocorrelation functions and the phase-insensitive cross-correlation function, are zero. It is worthwhile to point out that when the source brightness $\mathcal{I} \equiv PT_0\rho_0^2/a_0^2 \gg 1$, the first term in the square brackets dominates, and Eq. (57) approaches the classical phase-sensitive cross correlation given in Eq. (48). However, when $\mathcal{I} \ll 1$, the second term is much larger than the first, resulting in a much stronger phase-sensitive cross correlation than permitted in a classical state. If the brightness is lowered to the limit in which there is on average much less than one photon each in the signal and the idler beams during a measurement interval, then the state of these SPDC outputs is well approximated by a dominant vacuum component plus a weak pair of entangled photons, viz., the biphoton state [17,65].

Note that outside its low-brightness and high-brightness asymptotic regions, the phase-sensitive cross-correlation function given in Eq. (57) is not cross-spectrally pure as we assumed in Eq. (14). So we cannot immediately apply the Eq. (22) ghost image result. However, the squared magnitude of Eq. (57) is the sum of two cross-spectrally pure terms, so it is straightforward to derive the ghost image signature starting from Eqs. (11) and (12). Following this procedure and using the detection-plane phase-sensitive cross correlation, obtained by propagating each term in Eq. (57) according to Eq. (21), leads to the following result for the far-field ghost image:

$$\langle \hat{C}(\boldsymbol{\rho}_1)\rangle = C_0(\boldsymbol{\rho}_1) + \mathcal{C}_t^{(p)} \left(\frac{2P}{\pi a_L^2}\right)^2 e^{-2|\boldsymbol{\rho}_1|^2/a_L^2} \int_{\mathcal{A}_2} \mathrm{d}\boldsymbol{\rho} e^{-|\boldsymbol{\rho}_1+\boldsymbol{\rho}|^2/\rho_L^2} e^{-2|\boldsymbol{\rho}|^2/a_L^2} |T(\boldsymbol{\rho})|^2 + \sqrt{\frac{2}{\pi}} \frac{a_0^2}{PT_0\rho_0^2} \mathcal{C}_t^{(q)} \left(\frac{P}{\pi a_L^2}\right)^2 e^{-|\boldsymbol{\rho}_1|^2/a_L^2} \int_{\mathcal{A}_2} \mathrm{d}\boldsymbol{\rho} e^{-|\boldsymbol{\rho}_1+\boldsymbol{\rho}|^2/\rho_L^2} e^{-|\boldsymbol{\rho}|^2/a_L^2} |T(\boldsymbol{\rho})|^2, \tag{58}$$

where $C_0(\boldsymbol{\rho}_1)$ is given in Eq. (23), $\mathcal{C}_t^{(p)} = \mathcal{C}_t^{(n)}$ is as given in the previous subsections [see below Eq. (41)], and $\mathcal{C}_t^{(q)} \equiv 1/\sqrt{1+32/\Omega_B^2 T_0^2}$. Therefore, the ghost image obtained with SPDC is, in general, the superposition of two image-bearing terms. Nonetheless, in the two asymptotic limits of the source brightness $\mathcal{I}$, one image-bearing term is much stronger than the other. In particular, when $\mathcal{I} \gg 1$, the middle term in Eq. (58) dominates the last term, and the ghost image becomes approximately

$$\langle \hat{C}(\boldsymbol{\rho}_1)\rangle \approx C_0(\boldsymbol{\rho}_1) + \mathcal{C}_t^{(p)} \left(\frac{2P}{\pi a_L^2}\right)^2 e^{-2|\boldsymbol{\rho}_1|^2/a_L^2} \int_{\mathcal{A}_2} \mathrm{d}\boldsymbol{\rho} e^{-|\boldsymbol{\rho}_1+\boldsymbol{\rho}|^2/\rho_L^2} e^{-2|\boldsymbol{\rho}|^2/a_L^2} |T(\boldsymbol{\rho})|^2. \tag{59}$$

This image signature is *identical* to that obtained with classical phase-sensitive light. Hence in the limit of bright signal and idler outputs from SPDC, the ghost image approaches the *classical* limit.

In the low source-brightness limit, when $\mathcal{I} \ll 1$, we have that the last term in Eq. (58) dominates the middle image-bearing term, yielding the ghost image

$$\langle \hat{C}(\boldsymbol{\rho}_1) \rangle \approx C_0(\boldsymbol{\rho}_1) + \sqrt{\frac{2}{\pi}} \frac{a_0^2}{PT_0\rho_0^2} \mathcal{C}_t^{(q)} \left(\frac{P}{\pi a_L^2} \right)^2 e^{-|\boldsymbol{\rho}_1|^2/a_L^2} \int_{\mathcal{A}_2} \mathrm{d}\boldsymbol{\rho} e^{-|\boldsymbol{\rho}_1 + \boldsymbol{\rho}|^2/\rho_L^2} e^{-|\boldsymbol{\rho}|^2/a_L^2} |T(\boldsymbol{\rho})|^2. \tag{60}$$

The field of view of the source in this limit is given by $\sqrt{2}a_L$; i.e., it is a factor of $\sqrt{2}$ larger than that obtained with the two classical sources considered before. If we assume that the target and the pinhole scanning area are both well within this field-of-view, we can further simplify the image signature to

$$\langle \hat{C}(\boldsymbol{\rho}_1) \rangle = q^2 \eta^2 A_1 \left(\frac{2P}{\pi a_L^2} \right)^2 \times \left[\int_{\mathcal{A}_2} \mathrm{d}\boldsymbol{\rho} |T(\boldsymbol{\rho})|^2 + \frac{1}{\sqrt{8\pi}} \frac{a_0^2}{PT_0\rho_0^2} \mathcal{C}_t^{(q)} \int_{\mathcal{A}_2} \mathrm{d}\boldsymbol{\rho} e^{-|\boldsymbol{\rho}_1 + \boldsymbol{\rho}|^2/\rho_L^2} |T(\boldsymbol{\rho})|^2 \right], \tag{61}$$

which shows that the ghost image is a convolution of $|T(-\boldsymbol{\rho})|^2$ with the point-spread function $e^{-|\boldsymbol{\rho}|^2/\rho_L^2}$. In words, the far-field resolution achieved with this non-classical source equals those realized with the classical sources considered earlier, so, there is no quantum signature in the far-field image resolution.

The image contrast, however, has distinctly different behavior. Starting from Eq. (61), we find that the contrast factors into

$$\mathcal{C}^{(q)} \equiv \mathcal{C}_t^{(q)} \mathcal{C}_s^{(q)}, \tag{62}$$

where the temporal term $\mathcal{C}_t^{(q)}$ is defined above, and the spatial term is given by

$$\mathcal{C}_s^{(q)} = \frac{1}{\sqrt{8\pi}} \frac{a_0^2}{PT_0\rho_0^2} \frac{\max_{\boldsymbol{\rho}_1}[\mathcal{I}_q(\boldsymbol{\rho}_1)] - \min_{\boldsymbol{\rho}_1}[\mathcal{I}_q(\boldsymbol{\rho}_1)]}{\int_{\mathcal{A}_2} \mathrm{d}\boldsymbol{\rho} |T(\boldsymbol{\rho})|^2}, \tag{63}$$

with

$$\mathcal{I}_q(\boldsymbol{\rho}_1) \equiv \int_{\mathcal{A}_2} \mathrm{d}\boldsymbol{\rho} e^{-|\boldsymbol{\rho}_1 + \boldsymbol{\rho}|^2/\rho_L^2} |T(\boldsymbol{\rho})|^2 \tag{64}$$

being the point-spread degraded image of $|T(-\boldsymbol{\rho})|^2$. Using the previous assumption of a binary amplitude mask, we obtain

$$\mathcal{C}_s^{(q)} \approx \frac{1}{\sqrt{8\pi}} \times \frac{\pi a_L^2}{PT_0 A_T} \gg 1/PT_0 \tag{65}$$

because of our $\pi a_L^2/A_T \gg 1$ field-of-view assumption. Thus, in the broadband ($\Omega_B T_0 \ll 1$), low-brightness, low-flux limit, wherein the SPDC output becomes a dominant vacuum state plus a weak biphoton component, the image contrast becomes

$$\mathcal{C}^{(q)} \gg \Omega_B/P \gg 1\,, \tag{66}$$

where the last inequality follows from the low-flux condition. This is why biphoton-state ghost-imaging experiments have yielded background-free ghost images [1,9,10], despite SPDC's being a broadband process.

6. Signal-to-Noise Ratio

The low cross-correlation contrast of classical-state ghost images—which originates from the appreciable featureless background in which the desired image is embedded—is easily remedied by forming cross-covariance images, rather than cross-correlation images [9,10,17]. This can be accomplished by AC coupling the photocurrents into a correlator, or by background subtraction. Nevertheless, these techniques do not eliminate the shot noise and excess noise [69] associated with the featureless background, which affect the integration time needed to obtain an accurate cross-covariance estimate. Therefore it is important to quantify the performance of classical and quantum ghost imagers via their SNRs. Furthermore, pursuing closed-form analytic expressions for their SNRs is beneficial in identifying the most critical source and detector parameters that affect image quality.

In this section we will analyze the SNRs obtained with the three ghost-imaging sources that we have considered in the previous section. Unlike in the previous section, we will assume—for analytic simplicity—that AC coupling has been implemented to eliminate the background term $C_0(\boldsymbol{\rho}_1)$ seen in Eqs. (40), (50), and (58). We will also assume that the composite baseband frequency response of the photodetectors and their AC-coupling is given by the difference of two Gaussian functions [70],

$$H_B(\Omega) = \mathcal{F}[h_B(t)] = e^{-2\Omega^2/\Omega_B^2} - e^{-2\Omega^2/\Omega_N^2}, \tag{67}$$

where Ω_B is the baseband bandwidth of the detector as before, $\Omega_N \ll \Omega_B$ is the stopband bandwidth of the AC-coupling notch around $\Omega = 0$, and $\mathcal{F}[h_B(t)]$ denotes the Fourier transform of the composite filter's impulse response, $h_B(t)$. In order to minimize suppression of the baseband photocurrent fluctuations—whose cross correlation yields the ghost image—the notch bandwidth will be taken to be much smaller than the bandwidth of the impinging fields; i.e., $\Omega_N T_0 \ll 1$ will be assumed in all that follows.

In order to evaluate the ghost image SNR at $\boldsymbol{\rho}_1$, where

$$\mathrm{SNR} \equiv \frac{\langle \hat{C}(\boldsymbol{\rho}_1)\rangle^2}{\langle \Delta\hat{C}^2(\boldsymbol{\rho}_1)\rangle}, \tag{68}$$

and $\Delta\hat{C}(\boldsymbol{\rho}) \equiv \hat{C}(\boldsymbol{\rho}) - \langle \hat{C}(\boldsymbol{\rho})\rangle$, the variance term appearing in the denominator must be evaluated. This term can be expressed as

$$\langle \Delta\hat{C}^2(\boldsymbol{\rho}_1)\rangle = \frac{1}{T_I^2}\int_{-T_I/2}^{T_I/2} \mathrm{d}t \int_{-T_I/2}^{T_I/2} \mathrm{d}u \langle \hat{i}_1(t)\hat{i}_2(t)\hat{i}_1(u)\hat{i}_2(u)\rangle - \langle \hat{C}(\boldsymbol{\rho}_1)\rangle^2, \tag{69}$$

which reveals the primary challenge in evaluating the measurement variance: the fourth-moment of the photocurrents in the integrand is an eighth-order moment of the field operators. Fortunately, the moment-factoring theorem for Gaussian-state optical fields—which we used earlier in Section 3 to find $\langle \hat{C}(\boldsymbol{\rho}_1)\rangle$—allows all field moments to be expressed in terms of second-order moments. This procedure is straightforward but tedious, and we therefore confine our discussion to a description of the procedure, rather than a lengthy derivation. First, we express the integrand on the right-hand side of Eq. (69) in terms of the field-operator moments, as we have done in Eq. (11) for the mean. We then use the commutator relations, Eqs. (4) and (5), to put the integrand into normal order. This procedure yields the sum of four normally ordered field moments: one eighth-order moment, two sixth-order moments, and one fourth-order moment. Next, the Gaussian-state moment-factoring theorem is applied to each term, replacing higher-order moments with expressions that depend only on the second-order moments of the fields. Finally, by employing the coherence-separability of the correlation functions [71], the spatial and temporal integrals in each term are evaluated separately.

With all of the auto- and cross-correlation functions already specified in Section 5, evaluating the spatial and temporal integrals in the moment-factored variance expression is a straightforward exercise. For the spatial integrals, we assume that a_L exceeds the transverse extent of the transmission mask by an amount sufficient to permit the approximation $e^{-|\boldsymbol{\rho}|^2/a_L^2}|T(\boldsymbol{\rho})| \approx |T(\boldsymbol{\rho})|$. For convenience, we define

$$A_T' \equiv \int \mathrm{d}\boldsymbol{\rho} |T(\boldsymbol{\rho})|^4, \tag{70}$$

which we will regard as the effective area of the transmission mask. Our A_T' interpretation follows by analogy with the case of a binary ($|T(\boldsymbol{\rho})| \in \{0,1\}$) mask, for which A_T' is the area over which $|T(\boldsymbol{\rho})| = 1$. With this interpretation we have that $A_T'/\pi\rho_L^2$ is approximately the number of spatial resolution cells in the ghost image [17]. We also note that the small-pinhole approximation introduced in the previous section requires $\rho_L^2/A_1 \gg 1$ for its validity in far-field operation. Finally, we identify the two assumptions employed in evaluating the variance expression's temporal integrals: $T_I \gg T_0$ and $\Omega_B T_I \gg 1$. Neither of these averaging-time conditions is at all surprising. The former states that we must average over many source coherence times to form a high-quality ghost image. The latter states that we must average over many photodetector response times to achieve this same purpose.

As a final note, we will evaluate the ghost-imaging SNR behavior that prevails under narrowband and broadband illumination conditions. A source state is said to be narrowband if $\Omega_B T_0 \gg 1$, so that the coherence time of the impinging field

state T_0 greatly exceeds the $\sim 1/\Omega_B$ integration time of the photodetectors. Conversely, a broadband source state is one that satisfies $\Omega_B T_0 \ll 1$, so that the source's coherence time is much shorter than the photodetector's integration time.

Using the procedure described above, the SNR can be derived in a closed—albeit complicated—form for each of the sources considered below. The full form of the SNR expressions are presented in previous work [24], but in this paper we opt to skip them. Instead, we limit our presentation to the low- and high-brightness asymptotic expressions, which are simpler to interpret and gain insight from.

6.1. Thermal-State Light

We first consider the ghost-image SNR in the narrowband limit ($\Omega_B T_0 \gg 1$) as a function of source brightness $\mathcal{I} \equiv PT_0\rho_0^2/a_0^2 = PT_0\rho_L^2/a_L^2$. The contributions to the measurement variance (the SNR denominator) can be written as the sum of three terms: the variance contribution coming from excess noise alone, that from shot noise alone, and a term arising from beating between excess noise and shot noise. As the source brightness grows without bound, the SNR increases until it saturates at its maximum value,

$$\mathrm{SNR} = \sqrt{2\pi}\frac{T_I}{T_0}\frac{\rho_L^2}{A_T'}|T(\boldsymbol{\rho}_1)|^4, \tag{71}$$

for $A_T'/\rho_L^2 \gg 1$, which is limited by the excess-noise contribution [72]. Roughly speaking, this maximum SNR equals the number of source coherence times in the averaging interval divided by the number of spatial resolution cells in the image and multiplied by the square of the object's intensity transmission. Recall from Eq. (46) that $\pi\rho_L^2/A_T'$ is the image contrast for DC-coupled ghost-image formation in the far field with narrowband thermal-state light and a binary transmission mask (for which $A_T = A_T'$). Hence, the SNR of AC-coupled, high-brightness, thermal-state ghost imaging is proportional to the image contrast realized by using the same setup with DC coupling.

In the low-brightness asymptote, i.e., when $\mathcal{I} \ll 1$, the shot-noise contribution dominates the SNR noise denominator, yielding an expression quadratic in photon-flux, i.e.,

$$\mathrm{SNR} = \frac{16\sqrt{2}}{\sqrt{\pi}}\frac{T_I}{T_0}\frac{\eta P A_1}{\Omega_B a_L^2}\eta\mathcal{I}|T(\boldsymbol{\rho}_1)|^2. \tag{72}$$

In Fig. 5(a) we have plotted the narrowband thermal-state ghost-imaging SNR, along with its high-brightness and low-brightness asymptotes, for several narrowband ghost-imaging scenarios.

We now turn our attention to broadband sources, which satisfy $\Omega_B T_0 \ll 1$, and we assume that the ghost imager resolution satisfies $A_T'/\rho_L^2 \gg 1$. Here, too, SNR increases with increasing source brightness until it reaches its maximum value,

Figure 5

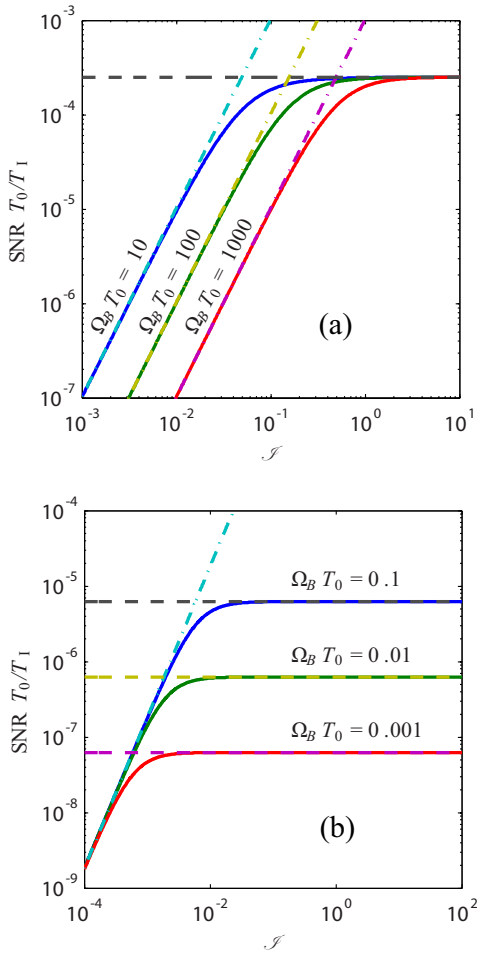

Thermal-state ghost-imaging SNR, normalized by T_I/T_0, plotted as a function of source brightness $\mathcal{I} \equiv PT_0\rho_0^2/a_0^2 = PT_0\rho_L^2/a_L^2$, for a far-field configuration ($\pi a_0\rho_0/\lambda_0 L \ll 1$) with $|T(\boldsymbol{\rho}_1)|=1$, $A_T'/\rho_L^2 = 10^4$, $\rho_L^2/A_1 = 10$, and $\eta = 0.9$. Various $\Omega_B T_0$ values are shown in the (a) narrowband and (b) broadband limits. Dashed–dotted lines represent low-brightness asymptotes, and dashed lines correspond to high-brightness asymptotes.

$$\mathrm{SNR} = \frac{\sqrt{\pi}}{2\sqrt{2}}\Omega_B T_I \frac{\rho_L^2}{A_T'}|T(\boldsymbol{\rho}_1)|^4, \tag{73}$$

where it is limited by excess noise alone. At very low source brightness, the SNR of the broadband thermal-state ghost imager becomes limited by shot noise alone and is given by

$$\mathrm{SNR} = \frac{4}{\sqrt{\pi}}\Omega_B T_I \frac{\eta P A_1}{\Omega_B a_L^2}\eta\mathcal{I}|T(\boldsymbol{\rho}_1)|^2. \tag{74}$$

Figure 5(b) shows several plots of broadband thermal-state ghost-imaging SNR, together with its high-brightness and low-brightness asymptotes. Aside from insignificant numerical factors, the broadband SNR expressions differ from the narrowband SNR expressions only through replacement of $1/T_0$ from the nar-

rowband expression with Ω_B in the broadband expression. This replacement is to be expected. In the narrowband case T_I/T_0 is the number of photocurrent coherence times that are being averaged by the correlator. This is because the narrowband condition $\Omega_B T_0 \gg 1$ ensures that the photon-flux fluctuations are not affected by the photodetector's baseband bandwidth limit. However, under the broadband condition, $\Omega_B T_0 \ll 1$, the photocurrent fluctuations have a much longer ($\sim 1/\Omega_B$) coherence time than that of the photon flux illuminating the detectors, so it is $\Omega_B T_I$ that appears in the broadband SNR formulas.

6.2. Classically Correlated Phase-Sensitive Light

For phase-sensitive coherence, the far-field regime corresponds to $\pi a_0^2/\lambda_0 L \ll 1$. As stated in Section 4, the only difference between the classical far-field phase-sensitive and phase-insensitive Gaussian-Schell model correlation functions is the swapping of $|\boldsymbol{\rho}_2+\boldsymbol{\rho}_1|^2$ and $|\boldsymbol{\rho}_2-\boldsymbol{\rho}_1|^2$. It follows that the far-field SNR expressions for classical phase-sensitive light are obtained from their phase-insensitive counterparts—Eqs. (71) and (72) for narrowband case and Eqs. (73) and (74) for the broadband case—by using $|T(-\boldsymbol{\rho}_1)|$ in lieu of $|T(\boldsymbol{\rho}_1)|$.

6.3. Maximally Entangled Phase-Sensitive Light

To evaluate the entangled source's ghost-image SNR in the far-field regime ($\pi a_0^2/\lambda_0 L \ll 1$) we utilize the same approximations that we have used for classical phase-sensitive light, but now we use the cross-correlation function from Eq. (57) in lieu of Eq. (48) when integral expressions are explicitly evaluated. The full closed-form solution for the SNR, which is derived by following the procedure described earlier in this section, is plotted for several scenarios in Fig. 6. Each of these plots captures the full quantum-to-classical transition seen in ghost imaging with maximally entangled phase-sensitive light (the output fields from SPDC) as the source brightness—mean photon-number per spatiotemporal mode—increases.

We begin our survey of the SNR results with the narrowband case. When the source is bright, i.e., $\mathcal{I} \gg 1$, the SNR equals that obtained with narrowband, bright, classical, and maximally correlated phase-sensitive light; i.e., it equals

$$\mathrm{SNR} = \sqrt{2\pi}\frac{T_I}{T_0}\frac{\rho_L^2}{A_T'}|T(-\boldsymbol{\rho}_1)|^4. \tag{75}$$

For dim-source ($\mathcal{I} \ll 1$) ghost imaging with $|T(-\boldsymbol{\rho}_1)| \sim 1$, the SNR becomes linear in photon flux,

$$\mathrm{SNR} = \frac{8}{\pi}\frac{T_I}{T_0}\frac{\eta^2 P A_1 |T(-\boldsymbol{\rho}_1)|^2}{\Omega_B a_L^2}. \tag{76}$$

In this regime the SNR is limited by the very low number of photon pairs detected over a detector integration time. The SNR achieved with narrowband maximally entangled phase-sensitive light is plotted in Fig. 6(a) for several $\Omega_B T_0$ values. The plots verify the linear low-brightness regime and the high-brightness saturation towards the classical asymptote. However, as shown in the plotted curves, the SNR can exceed the bright-source asymptote. When this occurs, there is a finite source brightness that yields the maximum SNR, and increasing

Figure 6

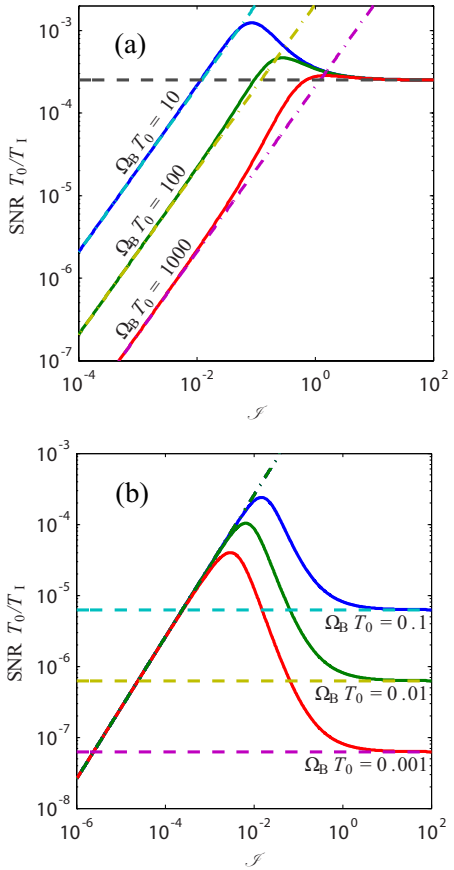

Nonclassical phase-sensitive Gaussian-state ghost-imaging SNR, normalized by T_I/T_0, plotted versus source brightness $\mathcal{I} \equiv PT_0\rho_0^2/a_0^2 = PT_0\rho_L^2/a_L^2$ for a far-field configuration $(\pi a_0^2/\lambda_0 L \ll 1)$ with $|T(-\boldsymbol{\rho}_1)| = 1$, $A_T'/\rho_L^2 = 10^4$, $\rho_L^2/A_1 = 10$, and $\eta = 0.9$. Various $\Omega_B T_0$ values are shown in the (a) narrowband and (b) broadband limits. Dashed–dotted lines represent low-brightness asymptotes, and dashed lines correspond to high-brightness asymptotes.

$\mathcal{I}$ beyond this threshold will *decrease* the SNR with increasing photon flux.

If the low-brightness condition on the source ($\mathcal{I} \ll 1$) is augmented with the *low-flux* condition

$$\frac{\eta P A_T'}{\Omega_B a_L^2} \ll 1, \tag{77}$$

then the average number of photons per integration time impinging on either detector becomes much less than unity. It follows that the photodetectors can be replaced with non-photon-resolving photodetectors without appreciable loss in imaging functionality, thereby rendering the Fig. 1 ghost-imaging configuration equivalent to biphoton-state ghost imaging with coincidence-counting circuitry (instead of photocurrent correlation). Thus, narrowband biphoton-state ghost imaging is also governed by the linear photon-flux SNR formula from Eq. (76) for $|T(-\boldsymbol{\rho}_1)| \sim 1$. In the biphoton regime, we can interpret $\eta^2 P A_1 |T(-\boldsymbol{\rho}_1)|^2/\Omega_B a_L^2$ as the mean number of photon coincidences per integration time of the detector,

which is then multiplied by the number of coherence intervals within the integration window, T_I/T_0, to obtain the final SNR expression.

Let us next shift our attention to the broadband ($\Omega_B T_0 \ll 1$) limit. When $\mathcal{I} \gg 1$, the SNR approaches the SNR of classical ghost imaging with a bright, phase-sensitive, and maximally correlated broadband source, i.e.,

$$\mathrm{SNR} = \frac{\sqrt{\pi}}{2\sqrt{2}} \Omega_B T_I \frac{\rho_L^2}{A_T'} |T(-\boldsymbol{\rho}_1)|^4. \tag{78}$$

On the other hand, if the low-brightness condition, $\mathcal{I} \ll 1$, and the low-flux condition, as given in Eq. (77), are both satisfied, and $|T(-\boldsymbol{\rho}_1)| \sim 1$, then

$$\mathrm{SNR} = \frac{1}{\pi} \Omega_B T_I \frac{\eta^2 P A_1 |T(-\boldsymbol{\rho}_1)|^2}{\Omega_B a_L^2}. \tag{79}$$

This expression corresponds to the broadband biphoton-state SNR. It equals the product of the mean number of coincidences per photodetector integration time multiplied by the number of independent observations within the integration window, $\Omega_B T_I$. As in the narrowband case, the SNR in this regime suffers from the paucity of photon pairs detected within the photodetector's $\sim 1/\Omega_B$ integration time, which is compensated by averaging the photocurrent product over many temporal coherence bins, i.e., employing $T_I \Omega_B \gg 1$. Figure 6(b) shows plots of the SNR for several values of $\Omega_B T_0$. It is seen that the linear photon-flux dependence of the SNR extends well beyond the low-flux regime. Furthermore, the SNR achieved in the low-brightness regime [i.e., Eq. (79)] can exceed the bright classical-source asymptote given in Eq. (78). Similar to what we found for narrowband operation, the broadband SNR has a well-defined maximum achieved at finite source brightness. Increasing the brightness beyond this optimal value reduces the SNR, which ultimately converges to the SNR attained with classical sources. All three of these SNR regimes are clearly identifiable in the Fig. 6(b) SNR plots. For example, for $\Omega_B T_0 = 10^{-2}$, the SNR is linear in photon flux until $\mathcal{I} \approx 10^{-3}$, its maximum occurs at $\mathcal{I} \approx 10^{-2}$, and then the SNR decreases with increasing $\mathcal{I}$ until at $\mathcal{I} \approx 10$ it converges to the bright-source asymptote.

In summary, we have found that classical-state ghost imager SNRs (thermal-state and classical phase-sensitive Gaussian state) saturate—with increasing source brightness—to maximum values that are inversely proportional to the number of resolution cells on the imaged object. Biphoton-state ghost imagers were shown to have SNRs that are typically proportional to their low photon flux. However, our analysis revealed that as the source brightness increases beyond the biphoton regime, the SNR typically reaches a well-defined maximum, after which increasing flux *reduces* the SNR. This may seem counterintuitive, but it is consistent with the fact that the SNR must approach the bright classical-state SNR as the source brightness increases beyond unity. Because this classical-state limit is in general *lower* than the maximum of the SNR achieved at lower brightness values, the SNR must have a decreasing trend as source brightness increases without bound.

7. Image Acquisition Time

All of the SNR expressions in the previous section are proportional to the cross-correlation averaging time T_I, so it is meaningful to compare the averaging times required in order to achieve a desired SNR value with different ghost-imaging

sources. Note that because the far-field ghost image obtained from a (classical or quantum) source with phase-sensitive cross correlation is inverted, we shall compare the imaging time for a ghost image at the spatial coordinate $\boldsymbol{\rho}_1$ using a thermal-state source with that for a ghost image at the spatial coordinate $-\boldsymbol{\rho}_1$ using a source with phase-sensitive coherence.

It should be no surprise that if *all* parameters are set equal, the SNR of ghost imaging with an SPDC source is always greater than the SNR of a classical-state source, because the cross correlation between the two source beams is stronger in the former case. Furthermore, it follows from the results in the previous section that the image acquisition time is significantly shorter with the maximally entangled Gaussian-state source when $\mathcal{I} \ll 1$, but the acquisition times of the maximally entangled and maximally correlated (classical) ghost-imaging sources are similar when $\mathcal{I} \gg 1$.

Nonetheless, because the primary advantage of classical-state ghost imaging is the abundance of photon flux, it is more interesting to compare the SNRs when the source fluxes (and possibly other parameters) are allowed to vary. Let us first consider the case in which all parameters except photon flux are equal in the configurations of interest. Because the classical sources we have considered thus far (thermal light and classical phase-sensitive light) yield identical SNRs, we shall use $P^{(c)}$ to denote their photon fluxes, reserving $P^{(q)}$ for the photon flux of the maximally entangled (nonclassical) state. Likewise, the averaging time for the classical-state ghost imagers to achieve the desired SNR will be denoted $T_I^{(c)}$, while that for the entangled-state source will be designated $T_I^{(q)}$. Then, we obtain

$$\frac{T_I^{(q)}}{T_I^{(c)}} = \frac{\sqrt{\pi^3}}{x\sqrt{8}} \frac{\Omega_B a_L^2}{\eta^2 P^{(q)} A_1} \frac{\rho_L^2}{A_T'} |T(\boldsymbol{\rho}_1)|^2, \tag{80}$$

where $x=2$ in the narrowband ($\Omega_B T_0 \gg 1$) limit, and $x=1$ in the broadband ($\Omega_B T_0 \ll 1$) limit. In obtaining this expression we have assumed that the classical-state sources are bright enough to achieve the saturation SNR in Eqs. (71) and (73), but the quantum source is limited to low brightness; so the nonclassical signature of the source prevails. In general, the comparison may favor either source. However, in the biphoton-state (low-flux) limit with $|T(\boldsymbol{\rho}_1)| \sim 1$, Eq. (80) implies that $T_I^{(q)} \gg T_I^{(c)}$, i.e., the cross-correlation averaging time required for narrowband biphoton-state ghost imagers to achieve a desired SNR value is much longer than that for bright classical-state ghost imagers to do so, given that all other system parameters are equal. Nevertheless, in a very high-resolution ghost-imaging configuration, high illumination flux ($P^{(q)} A_T' / \Omega_B a_L^2 \gg 1$) may be achievable with low-brightness ($P^{(q)} T_0 \rho_0^2 / a_0^2 \ll 1$) and maximally entangled phase-sensitive Gaussian-state light. In this case Eq. (80) implies that the averaging time for the nonclassical-state ghost imager can be shorter than that for the classical-state ghost imager [73]. For example, $|T(\boldsymbol{\rho}_1)| = 1$, $A_T' / \rho_L^2 = 10^4$, $\Omega_B T_0 = 10^{-2}$, $P^{(q)} T_0 \rho_0^2 / a_0^2 = 10^{-3}$, and $\rho_L^2 / A_1 = 10$ will yield $T_I^{(q)} \approx T_I^{(c)} / 100\,\eta^2$.

Finally, we compare ghost imaging with a broadband biphoton state (low brightness and low flux) to that with a bright narrowband classical state. Denoting the parameters specific to the classical and quantum sources with the superscripts (c) and (q) respectively, we obtain

$$\frac{T_I^{(q)}}{T_I^{(c)}} = \sqrt{2\pi^3}\frac{\Omega_B^{(q)} a_L^2}{\eta^2 P^{(q)} A_T'}\frac{\rho_L^2}{A_1}\frac{|T(\boldsymbol{\rho}_1)|^2}{\Omega_B^{(q)} T_0^{(c)}}. \tag{81}$$

Because the last factor on the right is typically less than unity, for $|T(\boldsymbol{\rho}_1)| \sim 1$, whereas the remaining factors are greater than unity, the cross-correlation averaging time may favor either source state. As an example, consider $|T(\boldsymbol{\rho}_1)| = 1$, $A_T'/\rho_L^2 = 10^4$, $P^{(q)} T_0^{(q)} \rho_0^2 / a_0^2 = 10^{-6}$, $\rho_L^2/A_1 = 10$. Then a biphoton-state source with 1 THz bandwidth and a 1 MHz thermal-state source will result in $T_I^{(q)} \approx 8 \times 10^{-3} T_I^{(c)}/\eta^2$, which shows that the biphoton-state imager enjoys an enormous advantage in averaging time as compared with the classical-state imager when the quantum efficiency is not unduly low.

The conclusions to be drawn from our treatment of image-acquisition time are the following. We showed that with equal bandwidth sources, and all system parameters being equal unless otherwise noted, bright classical-state ghost imagers typically reach the desired SNR value with a much shorter averaging time than that needed by a biphoton-state ghost imager. Therefore, despite the biphoton state's yielding images with high contrast even in DC-coupled operation, its photon-starved nature makes the total time duration it requires to accumulate the ghost image far in excess of what is necessary with a bright classical-state source. Nevertheless, we saw that there is a broadband, low-brightness, high-flux regime of nonclassical phase-sensitive light that may get by with much shorter cross-correlation averaging times than those needed by bright classical-state imagers. The notable drawback to reaping this quantum advantage, however, is the necessity for high quantum efficiency photon-number resolving detectors. Finally, we showed that there is no clear winner between ghost imaging with a broadband biphoton state and a narrowband bright classical state.

8. Computational Ghost Imaging

At this juncture, it is worthwhile to review the underlying physics of thermal-state ghost imaging in terms of the correlation of intensity fluctuations in the signal and reference arms. It is well known that a partially coherent thermal-state optical beam (whether it is true thermal light or pseudothermal light) has a speckled transverse intensity profile that fluctuates in time, with the speckles approximately the size of the spatial coherence diameter (at the transverse plane of interest) and the fluctuations occurring on a time scale approximately equal to the coherence time, as exemplified in Fig. 7. Therefore, after 50:50 beam splitting and propagation through L meters of free space, identical speckle patterns are generated on the signal- and reference-arm detection planes. The pinhole detector in the signal arm is smaller than a coherence diameter; thus it observes the fluctuations in only *one* speckle cell. The reference-arm bucket photodetector, on the other hand, measures a weighted-sum of the fluctuations from *all* of the speckle cells, where the weights correspond to the photon-flux transmissivity of the mask at the transverse spatial position of each speckle cell. Hence, when the speckle fluctuations seen by the single-pixel detector are correlated with the photocurrent from the bucket detector, the strength of the correlation is proportional to the weight of the corresponding speckle-cell contribution to the bucket detector output. In other words, the correlation is proportional to the object's photon-flux transmissivity at the transverse position illuminated by the speckle cell whose fluctuations are being measured by the signal-arm pinhole detector.

Figure 7

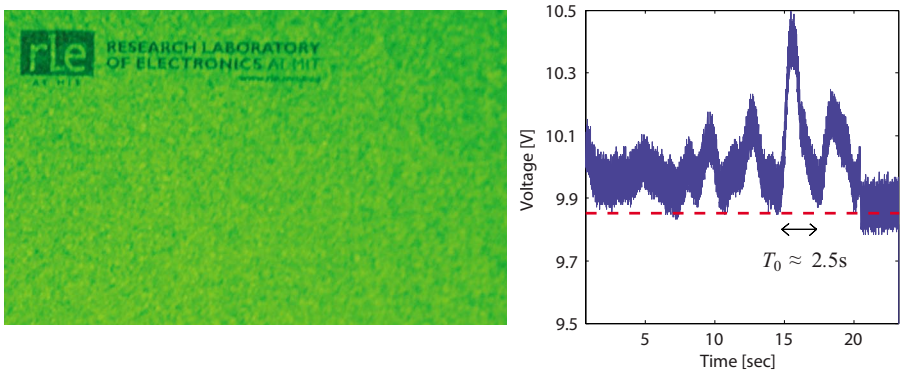

Spatiotemporal speckle of partially coherent light. (a) The transverse speckle pattern generated by illuminating a sheet of paper with a cw laser beam that has been rendered spatially incoherent by transmission through a ground-glass diffuser, and (b) the temporal fluctuations seen in a single speckle cell of a cw laser beam that has been transmitted through a rotating ground-glass diffuser. T_0 denotes the coherence time, and the dashed line (red) indicates the dark baseline.

We can now better appreciate the role of the signal arm in ghost imaging: the photocurrent from the pinhole detector provides a measurement of the intensity fluctuations occurring in one speckle cell on the detection plane. This measurement is critical in conventional thermal-state ghost imaging, because there is no *a priori* knowledge of the detector-plane speckle pattern that the thermal source will produce. It turns out, however, that imposing a deterministic spatiotemporal modulation on a coherent laser is a viable alternative to having true randomness in the source. In this case, because the intensity fluctuations are known *a priori*, the signal arm can be replaced with numerical computation.

To expand on this point, consider the configuration shown in Fig. 8. Here, we transmit a cw laser beam through a SLM whose inputs are chosen to create the

Figure 8

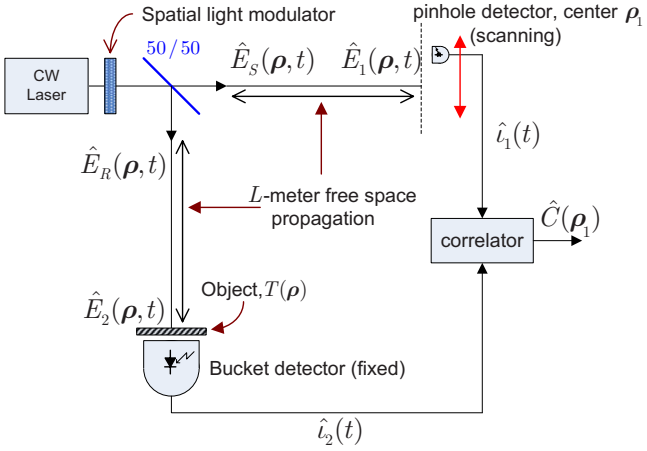

Ghost imaging with a cw laser and a SLM.

desired coherence behavior. Let us assume an idealized SLM consisting of $d \times d$ pixels arranged in a $(2M+1)\times(2M+1)$ array with 100% fill factor within a $D\times D$ pupil, where $D=(2M+1)d$ and $M\gg 1$. We use this SLM to impose a phase $\phi_{nm}(t)$ on the light transmitted through pixel (n,m).

Suppose we have that $\{e^{i\phi_{nm}(t)}: -M\le n,m\le M\}$ are independent identically distributed random processes obeying $\langle e^{i\phi_{nm}(t)}\rangle=0$ and $\langle e^{i[\phi_{nm}(t_2)-\phi_{jk}(t_1)]}\rangle = \delta_{jn}\delta_{km}e^{-|t_2-t_1|/T_0}$. These statistics prevail if, for example, $\{e^{i\phi_{nm}(t)}\}$ is a set of identically distributed random telegraph waves [74]. We focus on the narrowband case in which T_0 is long compared with the response time of the photodetectors, $1/\Omega_B$. After the beam splitter and the free-space propagation into the far field, the preceding source leads to zero-mean $\hat{E}_1(\boldsymbol{\rho},t)$ and $\hat{E}_2(\boldsymbol{\rho},t)$ with a phase-insensitive correlation function of the form given in Eq. (17), where $\mathcal{R}^{(n)}_{m,\ell}(t_2-t_1)=e^{-|t_2-t_1|/T_0}$ and

$$K^{(n)}_{m,\ell}(\boldsymbol{\rho}_1,\boldsymbol{\rho}_2) = \frac{P}{2}\left(\frac{d^2}{D\lambda_0 L}\right)^2 e^{ik_0(|\boldsymbol{\rho}_2|^2-|\boldsymbol{\rho}_1|^2)/2L} \times\left(\prod_{u=x,y}\frac{\sin(\pi d u_1/\lambda_0 L)}{\pi_0 d u_1/\lambda_0 L}\frac{\sin(\pi d u_2/\lambda_0 L)}{\pi d u_2/\lambda_0 L}\right) \times\left(\prod_{u=x,y}\frac{\sin[\pi D(u_1-u_2)/\lambda_0 L]}{\sin[\pi d(u_1-u_2)/\lambda_0 L]}\right), \tag{82}$$

where $m,\ell=1,2$. Although it is not a Gaussian–Schell form, the preceding spatial correlation function has an intensity width $\sim\lambda_0 L/d$ and a coherence length $\sim\lambda_0 L/D$, which is similar to our Section 5 conclusions, if we identify $d\approx\rho_0$ and $D\approx a_0$. Furthermore, using a central limit theorem argument, we can approximate the joint state of $\hat{E}_1(\boldsymbol{\rho},t)$ and $\hat{E}_2(\boldsymbol{\rho},t)$ as Gaussian. Hence the Fig. 8 configuration will produce a ghost image

$$\langle\hat{C}(\boldsymbol{\rho}_1)\rangle = q^2\eta^2 A_1\left(\int \mathrm{d}t h_B(t)\right)^2 K^{(n)}_{1,1}(\boldsymbol{\rho}_1,\boldsymbol{\rho}_1)\int_{\mathcal{A}_2}\mathrm{d}\boldsymbol{\rho}K^{(n)}_{2,2}(\boldsymbol{\rho},\boldsymbol{\rho})|T(\boldsymbol{\rho})|^2 + C_n\int_{\mathcal{A}_2}\mathrm{d}\boldsymbol{\rho}|K^{(n)}_{1,2}(\boldsymbol{\rho}_1,\boldsymbol{\rho})|^2|T(\boldsymbol{\rho})|^2, \tag{83}$$

where, once again, the first term is a featureless background that can be suppressed by means of a DC block, and the second term is the point-spread-function degraded image, which has spatial resolution $\lambda_0 L/D$ within a spatial region of width $\lambda_0 L/d$ [75].

The possibility of using noise generators to drive the SLM leads to the more interesting observation that *deterministic* near-orthogonal driving functions can be employed to achieve the same objective. The desired property at the SLM's output is a narrowband, zero-mean field state whose spatial coherence—inferred now from a time average, rather than an ensemble average, because there is no true randomness—is limited to field points within a single pixel. Employing sinusoidal modulation, $\phi_{nm}(t)=\Phi\cos[(\Omega_0+\Delta\Omega_{n,m})t]$, with a different $\Delta\Omega_{n,m}$ for each pixel is one possibility. Let $\langle\cdot\rangle_{T_I}$ denote time averaging over the T_I-second interval employed in obtaining the ghost image. We have that $\langle e^{i\phi_{n,m}(t)}\rangle_{T_I}\approx 2J_0(\Phi)\approx 0$ when $(\Omega_0+\Delta\Omega_{n,m})T_I\gg 2\pi$ and $\Phi\gg\pi$, where $J_0(\cdot)$ is the zeroth-order Bessel function of the first kind. With the additional condition $|\Delta\Omega_{n,m}|, |\Delta\Omega_{j,k}|\ll\Omega_0$, and $\Phi T_I|\Delta\Omega_{n,m}-\Delta\Omega_{j,k}|\gg 1$ when $(n,m)\ne(j,k)$, we have $\langle e^{i[\phi_{n,m}(t)-\phi_{jk}(t)]}\rangle_{T_I}\approx 0$, unless

$j=n$ and $k=m$. Finally, the narrowband requirement is met if the modulation periods $2\pi/(\Omega_0+\Delta\Omega_{n,m})$ are all much longer than the response time of $h_B(t)$. Thus, this deterministically modulated source will also yield a ghost image of spatial resolution $\lambda_0 L/D$ within a spatial region of width $\lambda_0 L/d$ embedded in a background that can be suppressed by means of a DC block.

At this point, the computational ghost-imaging configuration we introduce in Fig. 9 is easily understood. We use deterministic modulation of a cw laser beam to create the reference-arm field that illuminates the target transparency, and, as usual, we collect the light that is transmitted through the transparency with a bucket (single-pixel) detector. Knowing the deterministic modulation applied to the original cw laser beam allows us to use diffraction theory to *compute* the intensity pattern, $I_1(\boldsymbol{\rho}_1,t)\equiv\langle\hat{E}_1^\dagger(\boldsymbol{\rho}_1,t)\hat{E}_1(\boldsymbol{\rho}_1,t)\rangle$, that would have illuminated the pinhole detector in the usual lensless ghost-imaging configuration. Furthermore, we can subtract the time average of this intensity, in our computation, and eliminate the prevalent background term from the ghost image. To distinguish these computed values from actual light-field quantities, we will denote them $\tilde{I}_1(\boldsymbol{\rho}_1,t)$ and $\Delta\tilde{I}_1(\boldsymbol{\rho}_1,t)$, respectively. The time-and-ensemble averaged correlation function [76],

$$\langle\Delta\tilde{C}(\boldsymbol{\rho}_1)\rangle\equiv\left\langle\int \mathrm{d}\tau_1 q\,\eta A_1\Delta\tilde{I}_1(\boldsymbol{\rho}_1,t-\tau_1)h_B(\tau_1)\int \mathrm{d}\tau_2 q\,\eta P_2(t-\tau_2)h_B(\tau_2)\right\rangle_{T_I},\tag{84}$$

with $P_2(t)\equiv\int_{\mathcal{A}_2}\mathrm{d}\boldsymbol{\rho}\langle\hat{E}_2^\dagger(\boldsymbol{\rho},t)\hat{E}_2(\boldsymbol{\rho},t)\rangle$ being the ensemble-average photon flux illuminating the bucket detector, will then be a background-free ghost image—with spatial resolution $\lambda_0 L/D$ over a spatial extent of width $\lambda_0 L/d$—akin to what would be obtained from pseudothermal ghost imaging with $d\approx\rho_0$, $D\approx a_0$, and a DC block applied to the pinhole detector. It is worthwhile to emphasize that, because only one photodetector has been employed, it is *impossible* to interpret this computational ghost image as arising from nonlocal two-photon interference.

In summary, the Fig. 9 setup shows how ghost imaging can be performed with only a bucket (single-pixel) detector by precomputing the intensity fluctuation pattern that would have been seen by the scanning pinhole detector (or high-spatial-resolution camera). This computational ghost imager results in background-free images whose resolution and field of view can be controlled by choice of SLM parameters. Finally, this computational ghost-imaging configuration underscores the classical nature of ghost-image formation.

Figure 9

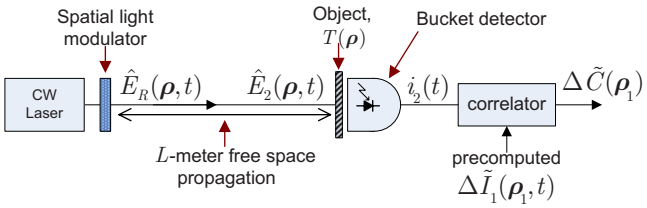

Computational ghost-imaging setup.

9. Discussion

Ghost imaging has captured the attention and interest of the quantum imaging community since its first demonstration with entangled photons over a decade ago. In Section 1 we summarized the theoretical and experimental milestones of ghost imaging prior to delving into its detailed treatment. The core of this paper was a development of the fundamental properties of the conventional dual-arm lensless ghost-imaging configuration. In particular, we analyzed the ghost image signature obtained with three classes of Gaussian-state sources. Two used classical-state light, specifically a joint signal-reference field state that has either the maximum phase-insensitive or the maximum phase-sensitive cross correlation consistent with having a proper P representation. The third used nonclassical light, in particular an entangled signal-reference field state, obtained from SPDC, with the maximum phase-sensitive cross correlation permitted by quantum mechanics. In Section 5 we examined ghost-imaging performance in the far field. There we showed that the nonclassical source yields a slightly larger field-of-view, but the resolution from all three sources are equal. Image contrast, however, is dramatically better with an SPDC source in its usual low-brightness operating regime. The SNR analysis we reported in Section 6 and the image-acquisition-time analysis presented in Section 7 showed that neither bright classical-state sources nor dim quantum sources universally yield superior SNR, or equivalently, shorter image-acquisition times. The particular source bandwidth, brightness, and resolution values determine which state gives better performance in these regards. We departed from the conventional dual-arm ghost-imaging setup in Section 8, where we showed that imposing a spatiotemporally varying deterministic modulation on a cw laser beam facilitates a single-arm ghost-imaging configuration (having only a single-pixel detector), in which the ghost image is extracted from the photodetector current via signal processing.

As our analysis in Section 3 shows, the fundamental source property that enables acquisition of a ghost image—whether the source is classical or quantum—is the nonzero cross covariance between the photon-flux densities of the two detected fields, i.e., the cross correlation of the photon-flux densities minus the product of their mean values. The product of the mean values generates a featureless background, while the cross covariance produces the image-bearing terms. For zero-mean Gaussian-state sources—including *both* thermal-state sources and the SPDC-generated biphoton-state sources—the point-spread function of the image is expressible as a sum of terms involving only the second-order moments of the field operators. As a result, we find that the phase-sensitive and phase-insensitive field-operator *cross correlations* are the primary Gaussian-state parameters that determine the ghost-image point-spread function. In [17] we showed that any pair of phase-sensitive and phase-insensitive cross-correlation functions can be obtained, in principle, from two classical Gaussian-state fields, so long as there are no restrictions on these fields' autocorrelation functions. In this respect, the image-bearing term alone does not contain any quantum signature *per se*. However, if we compare sources that have identical autocorrelation functions (thus, identical ghost-image backgrounds in DC-coupled operation), we find that nonclassical fields with low brightness and maximum phase-sensitive cross correlation offer a higher contrast image (when DC-coupling is used), a higher SNR, and some field-of-view expansion in the far field. We found that classical-state ghost imager SNRs saturate—with increasing source brightness—to a maximum value that is inversely proportional

to the number of resolution cells in the imaged object. In this high-brightness limit the classical ghost-imaging SNR is thus proportional to the contrast achieved in DC-coupled operation. The contrast can be improved by removing the featureless background via AC-coupled photodetectors or background subtraction, but SNR improvements, at high source brightness, require increasing the cross-correlation averaging time.

Although we consider the debate on the fundamentals of ghost imaging to be resolved, it is relevant to dispel some of the recent myths regarding the physics of thermal-state ghost imaging. In some recent publications it has been implied that ghost imaging with thermal-state light cannot be explained by classical electromagnetic theory in combination with semiclassical photodetection theory, but that nonlocal interference of photon pairs must be used to understand such experiments [15,31,77]. Although we have no dispute that all optical phenomena are fundamentally quantum mechanical, we strongly disagree that invoking nonlocal two-photon interference is compulsory to explain thermal-state ghost imaging. We have presented several explanations in this paper to support this view. First, we have reiterated the fact that a thermal state is a mixed state with a proper P representation, so classical stochastic-field electromagnetism combined with the semiclassical (shot noise) theory of photodetection yields thermal-state ghost-imaging predictions that are quantitatively identical to those obtained with quantum field operators and quantum photodetection theory. Second, and perhaps more critically, the proper P representation also implies that there is no nonlocal interaction in thermal-light ghost imaging in the sense of violating the Clauser–Horne–Shimony–Holt inequality [78]. Computational ghost imaging, studied in Section 8, precisely demonstrates this point by utilizing a *single* detector, which eliminates all possibility of nonlocal interactions. [79]. Two distinct fields propagating paraxially in two different directions can exhibit spatiotemporal correlations on transverse planes that are equidistant from the source. This concept is both well known in and central to classical statistical optics [44,52]. The physical separation between the two measurement planes does not automatically imply a signature of nonlocality in quantum mechanics.

One significant component of our analysis is the source referred to as classical phase-sensitive light, and merits a discussion in its own right. Specifically, it is a two-beam Gaussian state with the maximum phase-sensitive cross correlation permissible in classical statistical optics. This classical state is critical to properly delineating the classical–quantum boundary in most quantum imagers (e.g., see [17,80,81]) because it represents the Gaussian state that is most *similar* to the nonclassical Gaussian state of the signal and idler outputs from SPDC [51,55], which is currently the primary source for obtaining biphotons (entangled photon pairs). As such, there is an intimate physical connection between the phase-sensitive and phase-insensitive coherence duality [63], and the duality between the partial entanglement of biphotons and the partial coherence of classical phase-insensitive fields [6]. In particular, the biphoton state is the low-brightness, low-flux limit of the zero-mean jointly Gaussian state with maximum phase-sensitive cross correlation and zero phase-insensitive cross correlation. In this limit, the biphoton wave function *is* the phase-sensitive cross-correlation function between the signal and reference fields (e.g., see [17]). Hence, the duality between biphoton wave function propagation and phase-insensitive coherence propagation is rooted in the duality between *phase-sensitive* and *phase-insensitive* coherence propagation. Because classical fields—such as classical phase-sensitive Gaussian-state light—may also have

phase-sensitive coherence, it is imperative to distinguish features that are due to the presence of this phase-sensitive correlation from those that *require* this phase-sensitive correlation to be stronger than what is possible with classical states. The following examples illustrate our point. When ghost imaging is performed with phase-sensitive light, image inversion occurs in the far field for both classical and quantum sources. This inversion is entirely due to the difference between the free-space propagation of phase-sensitive and phase-insensitive correlations, and it is not necessary for the phase-sensitive coherence to be stronger than classical. On the other hand, the high contrast of DC-coupled ghost images formed with SPDC light arises from that source's phase-sensitive cross correlation's being much stronger than the classical limit, and this feature is *not* reproducible with classical phase-sensitive light.

Because of its significance, it is worthwhile to briefly consider how classical phase-sensitive light may be generated. The key ingredient to generating two beams with a phase-sensitive cross correlation is utilizing a process that imparts phase-conjugate modulations on the two beams. Thus narrowband classical phase-sensitive light can be generated by dividing a cw laser beam with a 50:50 beam splitter and imposing complex-conjugate modulations on the two beams, for example, by using telecommunications-grade electro-optic modulators. To obtain broadband classical phase-sensitive light one could utilize SPDC, but have thermal-state signal and idler inputs (instead of the vacuum-state inputs used to obtain an entangled signal-idler output), such that the joint signal and idler output state is a classical zero-mean Gaussian state with a phase-sensitive cross correlation.

In addition, we emphasize that Gaussian-state analysis provides a robust and versatile framework for answering some of the most fundamental questions associated with developing practical ghost imagers. We have utilized the versatility of this framework in our prior work and in this paper to obtain quantitative and comparable performance metrics for classical and quantum ghost imagers, thus unambiguously delineating the classical and quantum features of ghost imaging. The same framework can be applied to other imaging configurations as well, thereby establishing a methodology for investigating the boundary between their classical and quantum behavior.

We close with a final brief summary of what we have presented. We have used Gaussian-state analysis to establish a unified treatment of classical and quantum ghost imaging. Our analysis has revealed that ghost-image formation is due to phase-sensitive and phase-insensitive cross-correlations between the signal and reference fields. Because arbitrary cross-correlations can be achieved by classical and quantum sources alike, image contrast and SNR are the only distinguishing features between classical and quantum behavior. In particular, a classical source with phase-sensitive cross-correlation can produce an image *identical* to that obtained with a biphoton source—up to a different contrast and hence SNR—even for ghost-imaging configurations that utilize lenses, mirrors, or other linear optical elements. If we compare ghost images from classical and quantum sources having identical autocorrelations, then the low-brightness limit of the nonclassical source, in general, yields a field-of-view enhancement in far-field operation, but the image resolution (which is governed by the source diameter) is unaffected.

Acknowledgments

The authors thank F. N. C. Wong for insightful discussions and for performing the speckle measurements whose results appear in Fig. 7. The research described in this paper was carried out at MIT with support from the U.S. Army Research Office MURI grant W911NF-05-0197, the W. M. Keck Foundation Center for Extreme Quantum Information Theory, and the DARPA Quantum Sensors Program. B. I. Erkmen's contribution to writing this paper was carried out at the Jet Propulsion Laboratory, California Institute of Technology, under a contract with the National Aeronautics and Space Administration.

References

1. T. B. Pittman, Y. H. Shih, D. V. Strekalov, and A. V. Sergienko, "Optical imaging by means of two-photon quantum entanglement," Phys. Rev. A **52**, R3429–R3432 (1995).
2. R. S. Bennink, S. J. Bentley, and R. W. Boyd, ""Two-photon" coincidence imaging with a classical source," Phys. Rev. Lett. **89**, 113601 (2002).
3. M. D'Angelo and Y. Shih, "Can quantum imaging be classically simulated?," arXiv.org, arXiv:quant-ph0302146v2 (2003).
4. A. Gatti, E. Brambilla, and L. A. Lugiato, "Entangled imaging and wave-particle duality: from the microscopic to the macroscopic realm," Phys. Rev. Lett. **90**, 133603 (2003).
5. R. S. Bennink, S. J. Bentley, R. W. Boyd, and J. C. Howell, "Quantum and classical coincidence imaging," Phys. Rev. Lett. **92**, 033601 (2004).
6. B. E. A. Saleh, A. F. Abouraddy, A. V. Sergienko, and M. C. Teich, "Duality between partial coherence and partial entanglement," Phys. Rev. A **62**, 043816 (2000).
7. A. F. Abouraddy, B. E. A. Saleh, A. V. Sergienko, and M. C. Teich, "Role of entanglement in two-photon imaging," Phys. Rev. Lett. **87**, 123602 (2001).
8. A. F. Abouraddy, B. E. A. Saleh, A. V. Sergienko, and M. C. Teich, "Entangled-photon Fourier optics," J. Opt. Soc. Am. B **19**, 1174–1184 (2002).
9. A. Gatti, E. Brambilla, M. Bache, and L. A. Lugiato, "Correlated imaging, quantum and classical," Phys. Rev. A **70**, 013802 (2004).
10. A. Gatti, E. Brambilla, M. Bache, and L. A. Lugiato, "Ghost imaging with thermal light: comparing entanglement and classical correlation," Phys. Rev. Lett. **93**, 093602 (2004).
11. Y. Cai and S.-Y. Zhu, "Ghost imaging with incoherent and partially coherent light radiation," Phys. Rev. E **71**, 056607 (2005).
12. Y. Cai and S.-Y. Zhu, "Ghost interference with partially coherent light radiation," Opt. Lett. **29**, 2716–2718 (2004).
13. A. Valencia, G. Scarcelli, M. D'Angelo, and Y. Shih, "Two-photon imaging with thermal light," Phys. Rev. Lett. **94**, 063601 (2005).
14. F. Ferri, D. Magatti, A. Gatti, M. Bache, E. Brambilla, and L. A. Lugiato, "High-resolution ghost image and ghost diffraction experiments with thermal light," Phys. Rev. Lett. **94**, 183602 (2005).
15. G. Scarcelli, V. Berardi, and Y. Shih, "Can two-photon correlation of chaotic light be considered as correlation of intensity fluctuations?" Phys. Rev. Lett. **96**, 063602 (2006).

16. L. Basano and P. Ottonello, "A conceptual experiment on single-beam coincidence detection with pseudothermal light," Opt. Express **19**, 12386–12394 (2009).
17. B. I. Erkmen and J. H. Shapiro, "Unified theory of ghost imaging with Gaussian-state light," Phys. Rev. A **77**, 043809 (2008).
18. J. H. Shapiro, "Computational ghost imaging," Phys. Rev. A **78**, 061802(R) (2008).
19. Y. Bromberg, O. Katz, and Y. Silberberg, "Ghost imaging with a single detector," Phys. Rev. A **79**, 053840 (2009).
20. O. Katz, Y. Bromberg, and Y. Silberberg, "Compressive ghost imaging," Appl. Phys. Lett. **95**, 113110 (2009).
21. A. Gatti, M. Bache, D. Magatti, E. Brambilla, F. Ferri, and L. A. Lugiato, "Coherent imaging with pseudo-thermal incoherent light," J. Mod. Opt. **53**, 739–760 (2006).
22. B. E. A. Saleh and M. C. Teich, *Noise in Classical and Quantum Photon-Correlation Imaging* (SPIE, 2008), Vol. 183, Chap. 21.
23. J. Cheng and S.-S. Han, "Theoretical analysis of quantum noise in ghost imaging," Chin. Phys. Lett. **22**, 1676–1679 (2005).
24. B. I. Erkmen and J. H. Shapiro, "Signal-to-noise ratio of Gaussian-state ghost imaging," Phys. Rev. A **79**, 023833 (2009).
25. M. Bache, E. Brambilla, A. Gatti, and L. A. Lugiato, "Ghost imaging using homodyne detection," Phys. Rev. A **70**, 023823 (2004).
26. A. F. Abouraddy, P. R. Stone, A. V. Sergienko, B. E. A. Saleh, and M. C. Teich, "Entangled-photon imaging of a pure phase object," Phys. Rev. Lett. **93**, 213903 (2004).
27. X.-H. Chen, Q. Liu, K.-H. Luo, and L.-A. Wu, "Lensless ghost imaging with true thermal light," Opt. Lett. **34**, 695–697 (2009).
28. M. Bache, D. Magatti, F. Ferri, A. Gatti, E. Brambilla, and L. A. Lugiato, "Coherent imaging of a pure phase object with classical incoherent light," Phys. Rev. A **73**, 053802 (2006).
29. M. Zhang, Q. Wei, X. Shen, Y. Liu, H. Liu, J. Cheng, and S. Han, "Lensless Fourier-transform ghost imaging with classical incoherent light," Phys. Rev. A **75**, 021803(R) (2007).
30. J. Cheng, "Transfer functions in lensless ghost-imaging systems," Phys. Rev. A **78**, 043823 (2008).
31. R. Meyers, K. S. Deacon, and Y. Shih, "Ghost-imaging experiment by measuring reflected photons," Phys. Rev. A **77**, 041801(R) (2008).
32. R. E. Meyers, K. S. Deacon, and Y. Shih, "Quantum imaging of an obscured object by measurement of reflected photons," Proc. SPIE **7092**, 70920E (2008).
33. J. Cheng, "Ghost imaging through turbulent atmosphere," Opt. Express **17**, 7916–7921 (2009).
34. L. Wang, S. Qamar, S.-Y. Zhu, and M. S. Zubairy, "Hanbury Brown-Twiss effect and thermal light ghost imaging: a unified approach," Phys. Rev. A **79**, 033835 (2009).
35. M. H. Rubin and Y. Shih, "Resolution of ghost imaging for nondegenerate spontaneous parametric down-conversion," Phys. Rev. A **78**, 033836 (2008).
36. K. Chan, M. N. O'Sullivan, and R. W. Boyd, "Two-color ghost imaging," Phys. Rev. A **79**, 033808 (2009).
37. Q. Liu, X.-H. Chen, K.-H. Luo, W. Wu, and L.-A. Wu, "Role of multiphoton

bunching in high-order ghost imaging with thermal light sources," Phys. Rev. A **79**, 053844 (2009).
38. L.-H. Ou and L.-M. Kuang, "Ghost imaging with third-order correlated thermal light," J. Phys. B **40**, 1833–1844 (2007).
39. K. W. C. Chan, M. N. O'Sullivan, and R. W. Boyd, "High-order thermal ghost imaging," in *Conference on Lasers and Electro-Optics/International Quantum Electronics Conference*, OSA Technical Digest (CD) (Optical Society of America, 2009), paper JTuD100.
40. I. Agafonov, M. Chekhova, T. S. Iskhakov, and L.-A. Wu, "High-visibility intensity interference and ghost imaging with pseudo-thermal light," J. Mod. Opt. **56**, 422–431 (2009).
41. X.-H. Chen, I. N. Agafonov, K.-H. Luo, Q. Liu, R. Xian, M. V. Chekhova, and L.-A. Wu, "Arbitrary-order lensless ghost imaging with thermal light," arXiv.org, arXiv:0902.3713v1 [quant-ph] (2009).
42. The positive-frequency electric field operator is non-Hermitian; so both its phase-insensitive and phase-sensitive correlation functions must be specified in order to fully describe a zero-mean Gaussian state. This is discussed further in Section 4.
43. R. Loudon, *The Quantum Theory of Light*, 3rd ed. (Oxford Univ. Press, 2000).
44. L. Mandel and E. Wolf, *Optical Coherence and Quantum Optics* (Cambridge Univ. Press, 1995).
45. R. J. Glauber, "The quantum theory of optical coherence," Phys. Rev. **130**, 2529–2539 (1963).
46. R. M. Gagliardi and S. Karp, *Optical Communications* (Wiley, 1976).
47. J. H. Shapiro, "The quantum theory of optical communications," IEEE J. Sel. Top. Quantum Electron. **15**, 1547–1569 (2009).
48. J. H. Shapiro, "Corrections to "The Quantum Theory of Optical Communications" [Nov/Dec 09 1547-1569]," IEEE J. Sel. Top. Quantum Electron. **16**, 698 (2010).
49. We are assuming polarized light sources and targets that do not depolarize, so that scalar-wave theory suffices. The extension of our treatment to vector-wave sources and depolarizing targets is straightforward.
50. R. G. Gallager, *Discrete Stochastic Processes* (Kluwer Academic, 1996).
51. J. H. Shapiro, "Quantum Gaussian noise," in Proc. SPIE **5111**, 382–395 (2003).
52. J. W. Goodman, *Statistical Optics*, Classics ed. (Wiley, 2000).
53. H. P. Yuen and J. H. Shapiro, "Optical communication with two-photon coherent states—Part III: quantum measurements realizable with photoemissive detectors," IEEE Trans. Inf. Theory **26**, 78–92 (1980).
54. J. H. Shapiro, "Quantum measurement eigenkets for continuous-time direct detection," Quantum Semiclassic. Opt. **10**, 567–578 (1998).
55. J. H. Shapiro and K.-X. Sun, "Semiclassical versus quantum behavior in fourth-order interference," J. Opt. Soc. Am. B **11**, 1130–1141 (1994).
56. J. H. Shapiro, H. P. Yuen, and J. A. Machado Mata, "Optical communication with two-photon coherent states—Part II: photoemissive detection and structured receiver performance," IEEE Trans. Inf. Theory **25**, 179–192 (1979).
57. Strictly speaking, the quasi-monochromatic and paraxial conditions refer to the excited modes of the quantized field, i.e., all non-vacuum-state modes of the field operators $\hat{E}_S(\boldsymbol{\rho},t)e^{-i\omega_0 t}$ and $\hat{E}_R(\boldsymbol{\rho},t)e^{-i\omega_0 t}$ are confined to a

temporal-frequency bandwidth much smaller than ω_0 and a spatial-frequency bandwidth much smaller than ω_0/c.
58. H. P. Yuen and J. H. Shapiro, "Optical communication with two-photon coherent states—Part I: quantum state propagation and quantum noise reduction," IEEE Trans. Inf. Theory **24**, 657–668 (1978).
59. J. M. Wozencraft and I. M. Jacobs, *Principles of Communication Engineering* (Wiley, 1965).
60. In writing Eq. (23), we have used Eq. (16) to eliminate the temporal correlation terms.
61. Here ⋆ denotes convolution.
62. Because $\hat{E}(\boldsymbol{\rho},t)$ is a baseband field operator, Ω is the frequency detuning of the plane-wave component $\hat{A}(\mathbf{k},\Omega)$ from the wave's center frequency ω_0.
63. B. I. Erkmen and J. H. Shapiro, "Optical coherence theory for phase-sensitive light," Proc. SPIE **6305**, 63050G (2006).
64. Although it is more common to express the field of view as a solid angle, here we use the mean-square radius at the transverse target plane as our field-of-view measure.
65. F. N. C. Wong, T. Kim, and J. H. Shapiro, "Efficient generation of polarization-entangled photons in a nonlinear crystal," Laser Phys. **16**, 1517–1524 (2006).
66. E. Brambilla, A. Gatti, M. Bache, and L. A. Lugiato, "Simultaneous near-field and far-field spatial quantum correlations in the high-gain regime of parametric down-conversion," Phys. Rev. A **69**, 023802 (2004).
67. The SPDC output field operators presented herein are derived from quantized coupled-mode equations using the typical nondepleting plane-wave pump approximation. The transverse boundary effects within the crystal have been ignored, and unimportant global phase factors have been omitted.
68. Although the exact solution of the coupled-mode equations and the boundary conditions at the input facet of the nonlinear crystal does not lead to a Gaussian $\nu(\mathbf{k},\Omega)$, this assumption facilitates an analytic treatment without compromising the fundamental physics we are after.
69. Excess noise refers to fluctuations on the light illuminating the photodetectors that is transferred to the resulting photocurrents.
70. The filter $H_B(\Omega)$, including its AC coupling, will be assumed to be within the photodetector blocks shown in Fig. 1, so that $\langle \hat{i}_m(t)\rangle = 0$ for $m = 1,2$ for all the field states we shall consider.
71. Because the maximally entangled phase-sensitive cross-correlation function is not coherence separable, but rather a sum of two coherence-separable terms [see Eq. (57)], some extra steps are needed in evaluating the integrals in this case.
72. This is the same parametric dependence reported earlier in [21], without derivation.
73. It is necessary to utilize photon-number-resolving detectors in order to reap the advantages ascribed to this high-flux, low-brightness regime.
74. A. Papoulis, *Probability, Random Variables, and Stochastic Processes*, 3rd ed. (McGraw-Hill, 1991).
75. Recall that C_n is defined in Eq. (24).
76. The classical photocurrent measured by the bucket detector is a random process with shot-noise fluctuations. In deriving Eq. (84) we have used the ensemble average (mean) of the measured photocurrent, as we have done in all of the previous sections.

77. Y. Shih, "Quantum imaging," IEEE J. Sel. Top. Quantum Electron. **13**, 1016–1030 (2007).
78. J. F. Clauser, M. Horne, A. Shimony, and R. A. Holt, "Proposed experiment to test local hidden-variable theories," Phys. Rev. Lett. **23**, 880–884 (1969).
79. In our view, the interpretation of computational ghost imaging that suggests nonlocal interference between a physical photon in a light beam and a "virtual photon" arising from numerical computations on a computer processor—see M. H. Rubin, "Comment on ghost imaging with a single detector [arXiv0812.2633v2]," arXiv.org, arXiv:0902.1940v1 [quant-ph] (2009)—is far from being convincing, and is highly speculative.
80. B. I. Erkmen and J. H. Shapiro, "Phase-conjugate optical coherence tomography," Phys. Rev. A **74**, 041601(R) (2006).
81. B. I. Erkmen and J. H. Shapiro, "Gaussian-state theory of two-photon imaging," Phys. Rev. A **78**, 023835 (2008).

Baris I. Erkmen received his B.S., M.Eng and Ph.D. degrees in Electrical Engineering from MIT in 2002, 2003 and 2008, respectively. As a Master's student he participated in a project on high-data-rate atmospheric optical communications, utilizing spatial diversity reception and optical preamplification to mitigate the deleterious effects of turbulence. His M.Eng. thesis studied point-to-point atmospheric optical communication links in the near-field power transfer regime. Dr. Erkmen's doctoral research focused on the field of quantum imaging, and resulted in a unifying theory for classical and quantum imaging through the study of the coherence properties of phase-sensitive light. After his graduation, Dr. Erkmen was a Postdoctoral Scholar at MIT for a brief four months, after which he joined the Information Processing group at the Jet Propulsion Laboratory in Pasadena, California, as a Member of the Technical Staff. Dr. Erkmen's current research interests encompass the theoretical foundations of classical and quantum optical imaging, classical and quantum optical communications, remote sensing and estimation, and channel coding theory.

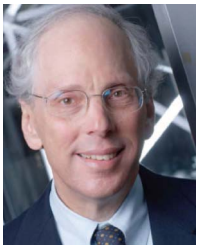

Jeffrey H. Shapiro is Director of the Research Laboratory of Electronics (RLE) at the Massachusetts Institute of Technology (MIT). He received the S.B., S.M., E.E., and Ph.D. degrees in Electrical Engineering from MIT in 1967, 1968, 1969, and 1970, respectively. As a graduate student he was a National Science Foundation Fellow, a Teaching Assistant, and a Fannie and John Hertz Foundation Fellow. His doctoral research was a theoretical study of adaptive techniques for improved optical communication through atmospheric turbulence. From 1970 to 1973, he was an Assistant Professor of Electrical Sciences and Applied Physics at Case Western Reserve University. From 1973 to 1985, he was an Associate Professor of Electrical Engineering at MIT, and in 1985, he was promoted to Professor of Electrical Engineering. From 1989 until 1999 Prof. Shapiro served as Associate Department Head of MIT's Department of Electrical Engineering and Computer Science. In 1999 he became the Julius A. Stratton Professor of Electrical Engineering. In 2001, Prof. Shapiro was appointed Director of RLE. Professor Shapiro's research interests have centered on

the application of communication theory to optical systems. He is best known for his work on the generation, detection, and application of squeezed-state light beams, but he has also published extensively in the areas of atmospheric optical communication, coherent laser radar, and quantum information science. Professor Shapiro is a Fellow of the Optical Society of America, of the American Physical Society, of the Institute of Electrical and Electronics Engineers, and of the Institute of Physics, and he is a member of SPIE (The International Society for Optical Engineering). In 2008 he was co-recipient of the Quantum Electronics Award from the IEEE Lasers and Electro-Optics Society, and he received the Quantum Communication Award for Theoretical Research from Tamagawa University. Professor Shapiro has been an Associate Editor of the IEEE Transactions on Information Theory and the Journal of the Optical Society of America, and was the Principal Organizer of the Sixth International Conference on Quantum Communication, Measurement and Computing (QCMC'02). He chaired the Steering Committee for the International Conferences on Quantum Communication, Measurement and Computing from 2008 until 2010, is currently Co-Director of the W. M. Keck Foundation Center for Extreme Quantum Information Theory (xQIT), and Co-Director of the Interdisciplinary Quantum Information Science and Engineering (iQuISE) Program.